Chapter 7

Neutrino Production and Searches for New Physics

In the previous chapter I described how I selected my samples of photonic events with missing energy. In this chapter I describe how I used these event samples to study the neutrino production at LEP and to search for manifestations of physics beyond the Standard Model.

Section 7.1 covers my measurements of the $e^+e^- \to \nu\bar{\nu}\gamma(\gamma)$ cross section and of the number of light neutrino species. In this section, I also discuss the systematic uncertainties in these measurements. In Sections 7.2 and 7.3, I describe my searches for Supersymmetry and for manifestations of large extra dimensions, respectively. Section 7.4 is devoted to measurements of gauge-boson couplings.

In the next chapter these results will be compared with results from other high-energy physics experiments. Finally, combinations of my results with those of the other LEP experiments are described in Appendix E.

7.1 Measurement of the Neutrino Production

As I described in Sections 6.3.8 and 6.4, both the single-photon and multi-photon samples were expected to consist almost purely of events from the neutrino pair-production accompanied by the emission of one or more photons, $e^+e^- \to \nu\bar{\nu}\gamma(\gamma)$. Therefore, to study this Standard Model process I used the combined single- and multi-photon event sample.

This combined sample consisted of 2,022 events selected in 1998-2000 L3 data that was in good agreement with the Monte Carlo expectation of 2,045 events, where 2,029 events were expected to come from the $e^+e^- \to \nu\bar{\nu}\gamma(\gamma)$ process and the rest from the background Standard Model processes and cosmic contamination. Thus, the purity of the combined $\nu\bar{\nu}\gamma(\gamma)$ sample was estimated to be 99.2%. Unless otherwise stated, in this chapter the Monte Carlo predictions for the $\mathrm{e}^+\mathrm{e}^-\to\nu\bar{\nu}\gamma(\gamma)$ process are obtained using the `KKMC` event generator, which was described in detail in Section 2.2.3.

7.1.1 Measurement of the $\mathrm{e}^+\mathrm{e}^-\to\nu\bar{\nu}\gamma(\gamma)$ cross section

The kinematic region of the combined single- and multi-photon selection corresponds to $14^\circ < \theta_\gamma < 166^\circ$ and $P_t^\gamma > 0.02\sqrt{s}$ or $P_t^{\gamma\gamma} > 0.02\sqrt{s}$ (see Section 6.2). The selection efficiency was then calculated as the ratio of the number of Monte Carlo events accepted after the full detector simulation and all analysis cuts to the total number of events generated within this phase space region. The obtained selection efficiency is given in Table 7.1 for each of the eight subsets of the L3 data used in my analysis.[1] The average selection efficiency was found to be 72.5%.

The cross section of the $\mathrm{e}^+\mathrm{e}^-\to\nu\bar{\nu}\gamma(\gamma)$ process ($\sigma_{\nu\bar{\nu}\gamma}^{meas}$) was then determined from the number of selected data events N_{data}, the number of expected background events N_{bg}, the selection efficiency ε, and the integrated luminosity $\mathcal{L}$, using the following formula:

$$\sigma_{\nu\bar{\nu}\gamma}^{meas} = \frac{N_{data} - N_{bg}}{\varepsilon\mathcal{L}} . \tag{7.1}$$

The measured and expected cross sections are listed in Table 7.1 and are shown as a function of $\sqrt{s}$ in Figure 7.1a. This figure also shows previous L3 measurements performed[2] with data collected at lower center-of-mass energies at the beginning of the LEP2 program [178].

To quantify possible deviations from the Standard Model expectations, I computed

---

[1] As discussed in Section 6.1, these eight subsets represent the data collected by the L3 detector during 1998-2000 at $\sqrt{s} = 189 - 208$ GeV. The corresponding integrated luminosities and center-of-mass energies were given in Table 6.1 (p. 132).

[2] These measurements were performed using a sample of 405 $\mathrm{e}^+\mathrm{e}^-\to\nu\bar{\nu}\gamma(\gamma)$ candidates selected in 88 pb^{-1} of data collected by L3 during 1995-1997 at $\sqrt{s} = 130 - 183$ GeV. The event selection is described in detail in Reference [58]. However, I re-evaluated the efficiency losses due to photon conversion using my measurements of the conversion probability (see Section 6.3.4). In addition, I used the more precise `KKMC` Monte Carlo generator which was not available at the time of the original publication [178]. It should be noted that the resulting corrections on the measured cross sections were not significant compared to the statistical precision of these measurements.

$\sqrt{s}$ (GeV)	$\varepsilon(\%)$	$\sigma_{\nu\bar{\nu}\gamma}^{meas}$(pb)	$\sigma_{\nu\bar{\nu}\gamma}^{exp}$(pb)	$\sigma_{\nu\bar{\nu}}^{meas}$(pb)	$\sigma_{\nu\bar{\nu}}^{exp}$(pb)
189	73.5	$4.86 \pm 0.19 \pm 0.05$	4.97	60.1 ± 2.5	61.6
192	72.6	$4.74 \pm 0.47 \pm 0.05$	4.77	60.4 ± 6.1	60.8
196	72.4	$4.52 \pm 0.27 \pm 0.05$	4.58	59.0 ± 3.6	59.8
200	71.9	$4.38 \pm 0.27 \pm 0.05$	4.39	58.7 ± 3.7	58.8
202	72.3	$4.78 \pm 0.44 \pm 0.05$	4.31	64.8 ± 6.0	58.4
205	72.0	$4.22 \pm 0.28 \pm 0.04$	4.20	58.1 ± 3.9	57.8
207	72.0	$3.98 \pm 0.21 \pm 0.04$	4.16	55.0 ± 2.9	57.5
208	71.8	$4.19 \pm 0.83 \pm 0.04$	4.13	58.1 ± 11.5	57.2

Table 7.1: Selection efficiency, measured and expected cross sections as a function of $\sqrt{s}$ for the $e^+e^- \rightarrow \nu\bar{\nu}\gamma(\gamma)$ process in the phase space region defined in the text. The first uncertainty on $\sigma_{\nu\bar{\nu}\gamma}^{meas}$ is statistical, the second systematic. The statistical uncertainty on the selection efficiency is 0.2% for each value of $\sqrt{s}$. The theoretical uncertainty on $\sigma_{\nu\bar{\nu}\gamma}^{exp}$ is 1% [24]. The last two columns give the measured and expected values of the extrapolated cross section for the $e^+e^- \rightarrow \nu\bar{\nu}(\gamma)$ process, where the error on $\sigma_{\nu\bar{\nu}}^{meas}$ is the quadratic sum of the statistical and systematic uncertainties.

the ratios of the measured and predicted cross sections at each center-of-mass energy as shown in Figure 7.1b. Averaging over the eight measurements yielded

$$R = \left\langle \frac{\sigma_{\nu\bar{\nu}\gamma}^{meas}}{\sigma_{\nu\bar{\nu}\gamma}^{exp}} \right\rangle = 0.987 \pm 0.022\,(stat) \pm 0.010\,(syst) \pm 0.010\,(theory)\,,$$

showing a good agreement between the data and the Standard Model predictions. This result also showed that while the total error was dominated by the statistical errors, the systematic and theoretical uncertainties could not be neglected. The total systematic uncertainty on the measured cross sections was estimated to be 1.1% for each value of $\sqrt{s}$ and was assumed to be almost fully correlated between all measurements. The sources of systematic errors will be described at the end of this section. The theoretical uncertainty on the predicted cross section was estimated to be 1% [24] as discussed in Section 2.2.3.

The measured $e^+e^- \rightarrow \nu\bar{\nu}\gamma(\gamma)$ cross section can then be extrapolated to the total

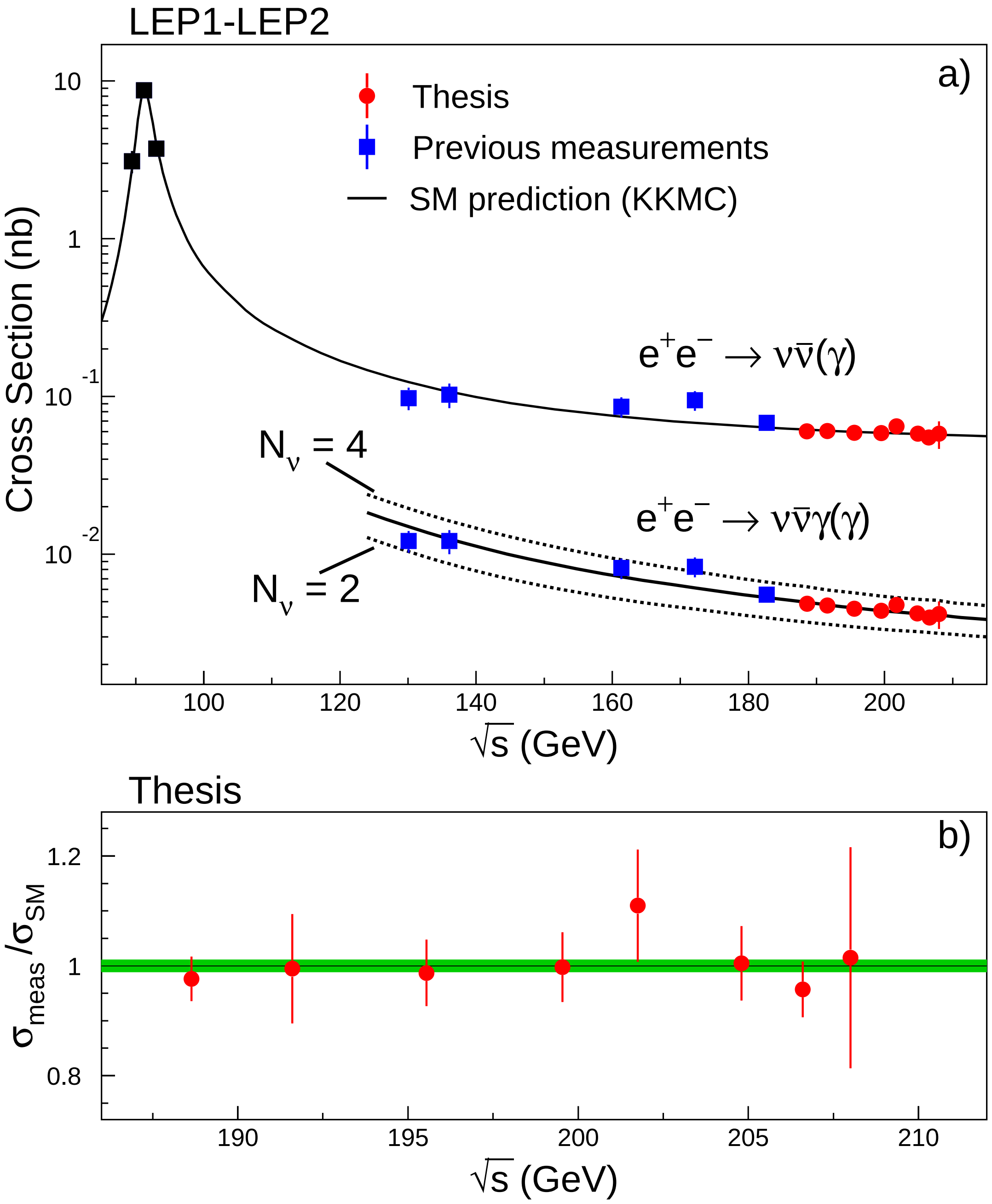

Figure 7.1: a) Cross sections of the $e^+e^- \rightarrow \nu\bar{\nu}(\gamma)$ and $e^+e^- \rightarrow \nu\bar{\nu}\gamma(\gamma)$ processes as a function of $\sqrt{s}$. The cross section of the latter process refers to the kinematic region defined in the text. The full line represents the theoretical prediction (`KKMC`) for $N_\nu = 3$ and the dashed lines are predictions for $N_\nu = 2$ and 4, as indicated. b) The ratio of the measured and the Standard Model predicted cross sections as a function of $\sqrt{s}$, where the error bars are the combined statistical and systematic uncertainties. The shaded region represents the theoretical uncertainty of 1% [24].

cross section of the neutrino pair-production process:

$$\sigma_{\nu\bar{\nu}}^{meas} = \sigma_{\nu\bar{\nu}\gamma}^{meas} \cdot \frac{\sigma_{\nu\bar{\nu}}^{exp}}{\sigma_{\nu\bar{\nu}\gamma}^{exp}}\,, \tag{7.2}$$

where $\sigma_{\nu\bar{\nu}}^{exp}$ is the predicted cross section of the $e^+e^- \rightarrow \nu\bar{\nu}(\gamma)$ process, obtained using the `KKMC` program. The results of this extrapolation are also listed in Table 7.1 and shown as a function of $\sqrt{s}$ in Figure 7.1a, which also shows results from previous measurements at LEP1 [179][3] and at the beginning of LEP2 [178].

Systematic Errors

The term *systematic error* is generally taken as signifying any error not due to statistical fluctuations in the data sample under study [180]. Therefore, the relative statistical and systematic errors on the measured $e^+e^- \rightarrow \nu\bar{\nu}\gamma(\gamma)$ cross section (see Equation 7.1) can be parametrized as

$$\begin{aligned} \frac{\delta_{stat}}{\sigma_{\nu\bar{\nu}\gamma}^{meas}} &= \frac{\sqrt{N_{data}}}{N_{data} - N_{bg}} && (7.3) \\ \frac{\delta_{syst}}{\sigma_{\nu\bar{\nu}\gamma}^{meas}} &= \sqrt{\left(\frac{\delta\varepsilon}{\varepsilon}\right)^2 + \left(\frac{\delta\mathcal{L}}{\mathcal{L}}\right)^2 + \left(\frac{\delta N_{bg}}{N_{data} - N_{bg}}\right)^2}\,, && (7.4) \end{aligned}$$

where the three terms arise from systematic errors on the selection efficiency $\delta\varepsilon$, the integrated luminosity $\delta\mathcal{L}$, and the background contamination δN_{bg}. Below I provide a detailed description of the main sources of these systematic errors.

Trigger efficiency: In Section 6.3.2 I determined the BGO trigger efficiency using a sample of single-electron events from the radiative Bhabha scattering process, $e^+e^- \rightarrow e^+e^-\gamma(\gamma)$. The corresponding error on the selection efficiency was then estimated to be $(\delta\varepsilon/\varepsilon)_{trig} = 0.6\%$, mainly due to the limited statistics of the single-electron sample. This estimate was further confirmed by an independent measurement of the trigger efficiency that I performed using back-to-back Bhabha events.

---

[3] The LEP1 measurements were performed using 100 pb^{-1} of data collected during 1991-1994 at $\sqrt{s} = 89.5 - 93.8$ GeV.

Photon conversion: In Section 6.3.4 I measured the rate of photon conversion in the dead material in front of the central tracker using samples of events from the $e^+e^- \to \gamma\gamma$ (barrel) and $e^+e^- \to \nu\bar{\nu}\gamma$ (endcaps) processes. The precision of this measurement was limited by statistics of these control samples, and the resulting error on the selection efficiency was then estimated to be $(\delta\varepsilon/\varepsilon)_{conv} = 0.5\%$. This estimate was found to be consistent with previous studies of this effect [120, 175].

Monte Carlo modelling: To estimate the systematic uncertainty due to modelling of the $e^+e^- \to \nu\bar{\nu}\gamma(\gamma)$ process, I determined the efficiency of my event selection using two independent Monte Carlo programs, `KKMC` and `NUNUGPV`. As discussed in Appendix A, these programs employ different algorithms to simulate higher-order QED corrections. In particular, the `KKMC` generator predicts a higher probability for the emission of additional ISR photons with finite, detectable transverse momentum. Since I rejected events with significant energy depositions in the forward calorimeters (see Section 6.3.3), the average selection efficiency was found to be slightly lower for `KKMC` than for `NUNUGPV`: $<\varepsilon>_{\mathtt{kkmc}} = 72.54 \pm 0.09\%$ and $<\varepsilon>_{\mathtt{nunugpv}} = 72.91 \pm 0.07\%$. I take the obtained relative difference in efficiency as the systematic uncertainty due to Monte Carlo modelling: $(\delta\varepsilon/\varepsilon)_{MC} = 0.5\%$. This estimate was found to be consistent with results of a similar study performed by the OPAL collaboration [181].

Monte Carlo statistics: The statistical error on the selection efficiency can be calculated as $\Delta\varepsilon = \sqrt{\varepsilon(1-\varepsilon)/N_{gen}}$, where N_{gen} is the number of Monte Carlo events generated within the kinematic region of my single- and multi-photon selection. The corresponding systematic uncertainty was then determined to be $(\delta\varepsilon/\varepsilon)^{MC}_{stat} = 0.3\%$. It should be noted that this uncertainty was uncorrelated between the eight data sets.

Shower-shape selection: The photon candidates were required to pass a set of cuts based on the shower profile measured in the BGO calorimeter. The performance of this shower-shape selection was studied in Section 6.3.1 using large samples of single-electron and back-to-back Bhabha events and cross checked using a control sample of di-photon events, $e^+e^- \to \gamma\gamma(\gamma)$. By comparing the efficiencies obtained with these independent samples and by varying the shower-shape cuts around the nominal values, I estimated the associated systematic uncertainty to be $(\delta\varepsilon/\varepsilon)_{shape} =$

0.3%. This estimate was also confirmed by a previous study of a similar shower-shape selection [58].

Background level: The background contamination from other Standard Model processes was dominated by the radiative Bhabha events. Such events were eliminated using a set of veto cuts on activity in the forward calorimeters. As described in Section 6.3.3, the veto efficiency was studied using a control sample of single-electron events and was found to be in good agreement with predictions of the detector simulation. The statistical precision of this measurement was then translated into an error on the number of expected background events, $\delta N_{bg} = 3$ events. Additional contributions came from the theoretical uncertainty on the $\mathrm{e}^+\mathrm{e}^- \rightarrow \mathrm{e}^+\mathrm{e}^-\gamma(\gamma)$ cross section (5% for the `TEEGG` generator [168]) and from uncertainties due to limited Monte Carlo statistics. Combining the above error sources, I estimated that the uncertainty on the level of background contributed about 0.2% to the total systematic error on the measured cross sections.

Luminosity: The systematic error on the integrated luminosity was estimated to be about $\delta\mathcal{L}/\mathcal{L} = 0.2\%$ [182]. It was dominated by the theoretical uncertainty on the accepted Bhabha cross section, by the uncertainty due to the selection procedure, and by the geometrical uncertainties in the position and alignment of the luminosity detectors (see Section 4.2.8). Therefore, the systematic error on the integrated luminosity was treated as common to all eight data sets that I used in my measurements [182].

Calorimeter geometry: An incorrect description of the geometry of the BGO calorimeter might lead to a systematic mismeasurement of the polar angle of the photon, which in turn might affect the cross section measurement. The difference of the definition of the polar angle between data and Monte Carlo was found to be less than 0.1° [183], translating to a systematic error of 0.2% on my cross section measurements.

Calorimeter calibration: As I described in Chapter 5, the BGO calorimeter was accurately calibrated using the RFQ calibration system. The BGO energy resolution was determined with a relative precision of about 15% (see Section 5.6.3). The error on the BGO energy scale was estimated by comparing the reconstructed masses of the π^0 and η mesons with their nominal values (see Figure 5.21) and by studying the effects of the BGO aging and non-linearity (see Appendix C). The resulting uncertainty on the photon energy scale was found to be less than 0.5%. I then varied the BGO energy scale and resolution within their errors during the detector simulation and assigned the observed shift in the selection efficiency to the systematic error due to the calorimeter calibration: $(\delta\varepsilon/\varepsilon)_{calib} = 0.1\%$.

Cosmic contamination: As described in Section 6.3.5, the cosmic ray background was studied using a control sample of out-of-time cosmic events and was expected to contribute only about 3 ± 1 events to the selected single- and multi-photon sample. I also took into account the uncertainty on the efficiency of the L3 scintillator system which was measured to a precision of about 0.05% using control samples of Bhabha and di-photon events. Combining these two error sources gave an additional systematic error of about 0.1% on the cross section measurement.

Detector noise: The noise in various subdetectors was studied using events randomly triggered at the beam crossing time (see Section 6.3.7). The resulting efficiency loss was estimated to be about 1.9%, and the Monte Carlo predictions were scaled accordingly. The statistical error on this correction factor (see Table 6.4) directly translated into a systematic error on the selection efficiency, $(\delta\varepsilon/\varepsilon)_{noise} = 0.1\%$.

The systematic errors on the measured cross sections are summarized in Table 7.2. Adding all contributions in quadrature, I obtained a total systematic error of 1.1%. As I discussed in Section 6.1, the same Monte Carlo models and calibration procedures were used throughout my analysis. Therefore, I assumed all systematic uncertainties, except that from Monte Carlo statistics, to be fully correlated when combining results obtained at different center-of-mass energies.

Source	Uncertainty (%)
Trigger efficiency	0.6
Photon conversion	0.5
Monte Carlo modelling	0.5
Monte Carlo statistics	0.3
Shower-shape selection	0.3
Background level	0.2
Luminosity	0.2
Calorimeter geometry	0.2
Calorimeter calibration	0.1
Cosmic contamination	0.1
Detector noise	0.1
Total	1.1

Table 7.2: Summary of the systematic uncertainties on the measurement of the $\mathrm{e^+e^-}\rightarrow \nu\bar{\nu}\gamma(\gamma)$ cross section, itemized by the source of uncertainty.

7.1.2 Determination of the Number of Light Neutrino Species

In the Standard Model of the electroweak interactions, the reaction $\mathrm{e^+e^-}\rightarrow \nu\bar{\nu}\gamma(\gamma)$ proceeds through s-channel Z exchange for all neutrino flavors ($\nu_l = \nu_\mathrm{e}, \nu_\mu, \nu_\tau$) and through t-channel W exchange for electron neutrinos only.[4] As a consequence, the cross section of this process depends linearly on the number of light neutrino species N_ν and can be written as

$$\sigma_{\nu\bar{\nu}\gamma} = N_\nu \cdot \sigma_Z + \sigma_{WZ} + \sigma_W \; , \tag{7.5}$$

where σ_Z, σ_{WZ}, and σ_W denote the contributions from the s-channel Z production, the W−Z interference, and the t-channel W exchange, respectively.

Figure 7.2 compares the recoil mass spectrum (M_rec) of the combined single- and multi-photon event sample to the expectations for $N_\nu = 2, 3$, and 4. The data clearly preferred the Standard Model value of $N_\nu = 3$. In order to quantify this agreement,

---

[4] The production mechanisms of this process as well as the expected cross sections and kinematic distributions have been examined in detail in Section 2.2 of Chapter 2 and in Appendix A.

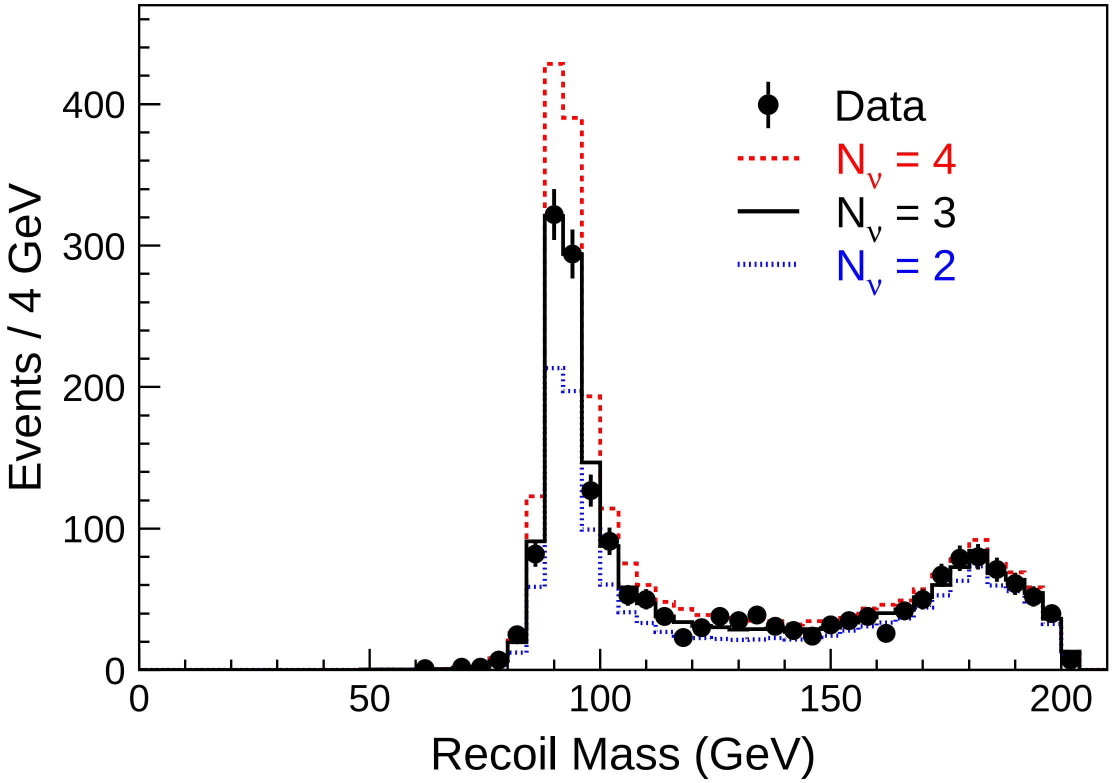

Figure 7.2: Recoil mass spectrum of the combined single- and multi-photon event sample, compared to the expected spectra for $N_\nu = 2, 3$ and 4.

I performed a binned fit to the two dimensional distribution of $M_{\rm rec}$ *vs.* $|\cos\theta_\gamma|$ of the selected $\nu\bar{\nu}\gamma(\gamma)$ events. Due to the different contributions from the t-channel $\nu_{\rm e}\bar{\nu}_{\rm e}\gamma$ production and the s-channel $\nu\bar{\nu}\gamma$ production, this method was more powerful than using the total cross section measurement. As shown in Figures 2.7c,d (p. 21), the s-channel Z exchange was expected to produce predominantly events in the region of the Z-return peak ($M_{\rm rec} \simeq M_Z$), whereas the W-related contributions dominated in the region of high recoil masses ($M_{\rm rec} \gtrsim 140$ GeV).

To determine the number of light neutrino species, I used the *method of maximum likelihood*. In the general case of binned data, the log-likelihood function is defined as [184]

$$\ln L = \sum_{m=1}^{N} k_m \ln \mu_m(\boldsymbol{\theta}) - \mu_{\rm m}(\boldsymbol{\theta})\,, \tag{7.6}$$

where N is the total number of bins, k_m is the number of events observed in bin m,

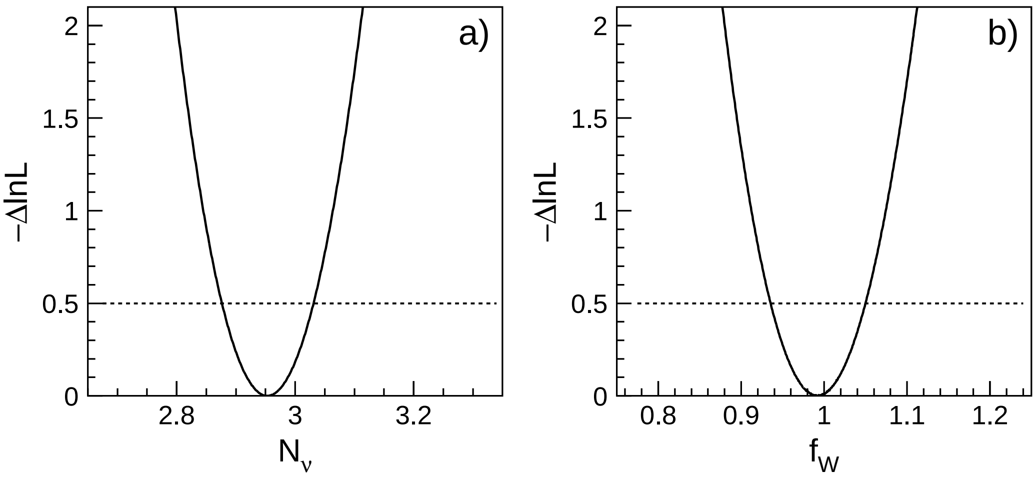

Figure 7.3: The negative log-likelihood functions of the fits for a) N_ν and b) f_{W}. The f_{W} measurement is described at the end of this section (p. 202).

$\mu_m(\boldsymbol{\theta})$ is the corresponding number of expected events, and $\boldsymbol{\theta}$ is the set of parameters which are allowed to vary in the fit. In this particular case, $\boldsymbol{\theta} = \{N_\nu\}$ and the expected number of events μ_m depended on N_ν according to Equation 7.5.

The number of light neutrino species was then determined by maximizing the log-likelihood function. As shown in Figure 7.3a, the obtained log-likelihood function was parabolic and the standard-deviation statistical error (δN_ν) was estimated by solving numerically the following equation:

$$\ln L(\hat{N}_\nu \pm \delta N_\nu) = \ln L(\hat{N}_\nu) - \frac{1}{2}\,, \tag{7.7}$$

where $\hat{N}_\nu$ denotes the fitted value of N_ν. The result of this maximum likelihood fit was

$$N_\nu = 2.95 \pm 0.08\,(stat) \pm 0.03\,(syst) \pm 0.03\,(theory)\,.$$

The systematic error was estimated by evaluating the shifts in the fitted value of N_ν associated with different sources of systematic uncertainties,[5] where the considered systematic effects were the same as for the cross section measurement (see Table 7.2).

---

[5] This method will be described in more detail in Section 7.4, where it will be used to estimate systematic errors in my measurements of gauge-boson couplings. It should be noted that this method was adopted by the W-physics group of L3 [185].

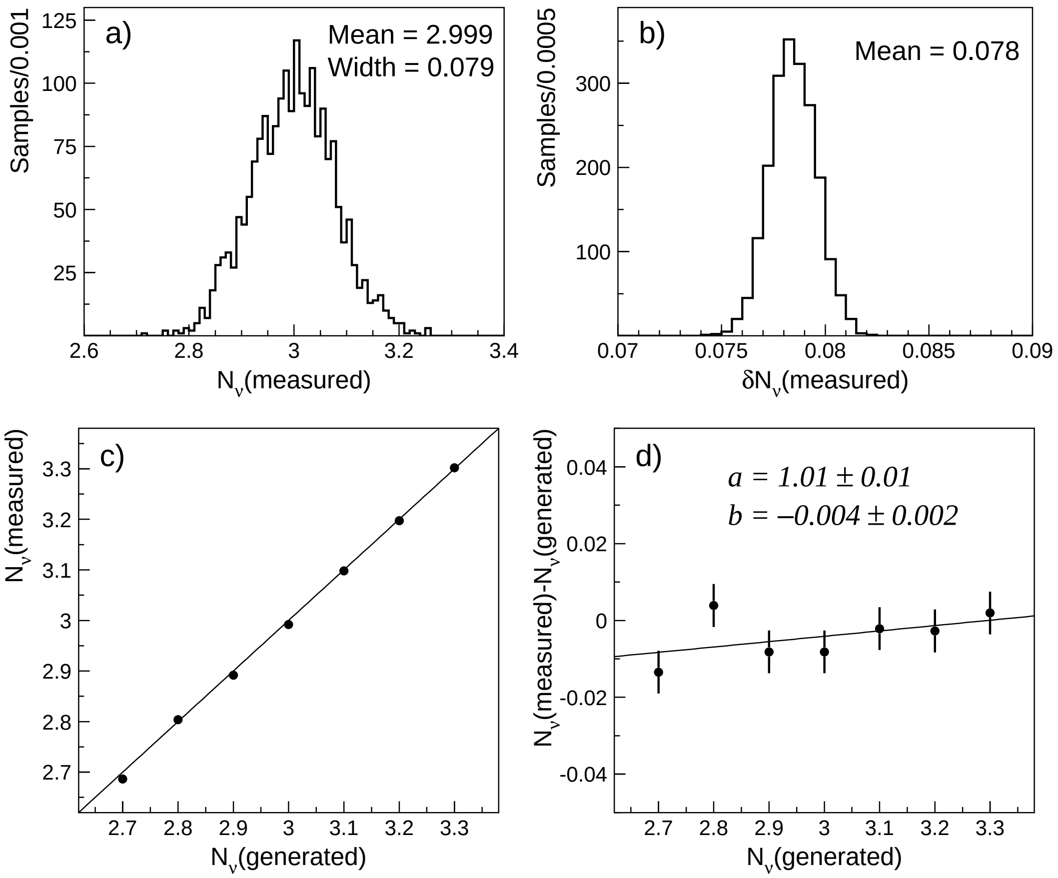

Figure 7.4: Distributions of a) the fitted values of N_ν and b) fit errors for small Monte Carlo samples corresponding to $N_\nu = 3$. The statistical parameters of interest are indicated on the plots. Results of the fit bias tests: c) the average fitted value of N_ν for small Monte Carlo samples with different N_ν, and d) the corresponding $N_\nu^{fit} - N_\nu^{gen}$ distribution. The statistical uncertainties on the averages and the results of the linear regression are also given.

The last uncertainty includes the theoretical uncertainty on the expected cross section [24] as well as an additional uncertainty on the shape of the recoil mass spectrum, estimated by comparing `KKMC` with `NUNUGPV`.

The performance of the fitting procedure was investigated with the standard Monte Carlo methods [184, 185]. First, I constructed small Monte Carlo samples by randomly combining Monte Carlo events in numbers given by the Poisson distribution around the expected number of events for a given value of N_ν. The reliability of the statistical error was then tested by fitting two thousand small Monte Carlo samples with the Standard Model value $N_\nu = 3$. The RMS width of the distribution of the fitted central values agreed well with the mean of the distribution of the fit uncertainties (see Figures 7.4a,b).

In order to check for any bias, I used Monte Carlo samples constructed for several different values of N_ν. The average fitted values (N_ν^{fit}) were compared to the "true" generated values (N_ν^{gen}), as shown in Figures 7.4c,d. This comparison was parameterized by a fit

$$(N_\nu^{fit} - 3) = a \cdot (N_\nu^{gen} - 3) + b\,, \tag{7.8}$$

which gave a linearity coefficient $a = 1.01 \pm 0.01$ compatible with 1 and a negligible bias $b = -0.004 \pm 0.002$. In addition, the fitting procedure was found to be stable with respect to changes in the bin size. Since the observed systematic effects were negligible compared to the total systematic error, no additional systematic errors were assigned as a result of these cross checks.

Combination with Previous Measurements

This result can be combined with measurements of the $\mathrm{e^+e^-} \to \nu\bar{\nu}\gamma(\gamma)$ process performed at the beginning of LEP2 and at LEP1. Using single- and multi-photon events selected in the data collected by L3 during 1995-97 at $\sqrt{s} = 130 - 183$ GeV, I obtained[6] $N_\nu = 3.23 \pm 0.18\,(stat) \pm 0.06\,(syst)$.

The LEP1 measurement [173, 179] was performed with a sample of 2,091 single-photon candidates selected in 100 pb^{-1} of data collected from 1991 to 1994 at energies near the Z resonance, $\sqrt{s} = 89.5 - 93.8$ GeV. Since the reaction $\mathrm{e^+e^-} \to \nu\bar{\nu}\gamma(\gamma)$ proceeded almost exclusively through s-channel Z exchange, the resulting photon energy spectrum was quite soft, $E_\gamma \simeq$ 1-4 GeV. The number of light neutrino species was then determined by fitting the total production cross section, measured as a function of $\sqrt{s}$. The fit result was $N_\nu = 2.98 \pm 0.07\,(stat) \pm 0.07\,(syst)$ [179]. As described in Chapter 4, the L3 detector was significantly upgraded at the end of the LEP1 program. In particular, the installation of the RFQ accelerator allowed me to

---

[6] The analysis of the $\sqrt{s} = 130 - 183$ GeV data was described in footnote 2 on page 190.

significantly improve the quality of the calorimeter calibration (see Chapter 5), which was one of the dominant sources of systematic uncertainty at LEP1.

To combine the above results with my measurement of N_ν, I used the `BLUE`[7] method [186] which allowed me to take into account correlations between the systematic uncertainties of these measurements.[8] The combination gave

$$N_\nu = 2.98 \pm 0.05\,(stat) \pm 0.04\,(syst)\,,$$

where the theoretical uncertainties were included in the total systematic error. This result is in agreement with the Standard Model prediction of $N_\nu = 3$ and is more precise than the present world average of measurements obtained by studying the reaction $\mathrm{e^+e^-} \to \nu\bar{\nu}\gamma(\gamma)$ [6]. It also agrees with the indirect measurement of invisible Z width at LEP1 ($N_\nu = 2.978 \pm 0.014$ [183]), while being sensitive to different systematic and theoretical uncertainties [179].

Study of the $\mathrm{e^+e^-} \to \nu_\mathrm{e}\bar{\nu}_\mathrm{e}\gamma(\gamma)$ Process

The selected sample of single- and multi-photon events could also be used to measure the size of the t-channel W exchange contributions in the reaction $\mathrm{e^+e^-} \to \nu_\mathrm{e}\bar{\nu}_\mathrm{e}\gamma(\gamma)$. These contributions were parameterized by a multiplicative scale factor f_W, defined to be 1 for the Standard Model expectation. The number of neutrino species was assumed to be equal to 3, as indicated by the above measurement. The cross section of the single- and multi-photon production process could then be written as

$$\sigma_{\nu\bar{\nu}\gamma} = 3 \cdot \sigma_Z + f_W \cdot (\sigma_{WZ} + \sigma_W)\,, \tag{7.9}$$

---

[7] The `BLUE` (Best Linear Unbiased Estimate) method is widely used in high-energy physics for combining correlated measurements such as W mass measurements at LEP [10] and Tevatron [187].

[8] Since the LEP1 and LEP2 measurements used different theoretical calculations and Monte Carlo generators, their theoretical uncertainties were assumed to be uncorrelated. The experimental systematic errors in both measurements were mainly due to limited statistics of various control samples. In addition, the LEP1 analysis considered only photons in the BGO barrel, whereas about half of the photon candidates used in the LEP2 analyses were in the BGO endcaps. As a consequence, the experimental systematic errors of the LEP1 and LEP2 measurements were also largely uncorrelated. The main sources of correlated systematic errors were: the integrated luminosity measurement, the description of the calorimeter geometry, and the simulation of the single-photon trigger near the threshold. On the contrary, the LEP2 measurements obtained with the 130 – 183 GeV and 189 – 208 GeV data were strongly correlated because they were performed using the same Monte Carlo programs and the same corrections for photon conversion effects.

with σ_Z, σ_{WZ}, and σ_W denoting the Standard Model predictions for the contributions from the s-channel Z production, the W−Z interference, and the t-channel W exchange,[9] respectively.

To measure the scale factor f_W, I used the same kinematic distribution and fitting procedure as for the N_ν measurement. However, in this case the contributions from the s-channel Z exchange constituted an important source of irreducible background. As a consequence, the f_W measurement mainly probed the recoil mass region above the Z-return peak, $M_{\text{rec}} \gtrsim 140$ GeV (see Figures 2.7c,d p. 21). The result of the binned maximum likelihood fit was

$$f_W = 0.99 \pm 0.06\,(stat) \pm 0.02\,(syst) \pm 0.02\,(theory)\,,$$

in good agreement with the Standard Model value $f_W = 1$. The obtained log-likelihood curve is shown in Figure 7.3b (p. 199). Contrary to the LEP1 measurement of $f_W = 0.2 \pm 0.6 \pm 0.4$ [173], this result clearly established that the W-contributions were observed and were consistent with the expectations from the Standard Model.

7.2 Searches for SUSY Signatures

Supersymmetry (SUSY) constitutes one of the most interesting and promising extensions of the Standard Model. The main aspects of this theory have been discussed in Chapter 3. Especially interesting are SUSY scenarios leading to production of neutralinos and gravitinos in e^+e^- collisions at LEP, as such processes can be detected by analyzing the selected samples of single- and multi-photon events. In this section I present the results of my searches for such SUSY signatures. The corresponding signal topologies and search strategies have been described in Section 3.2 of Chapter 3, to which I will frequently refer in the following discussion.

The kinematic cuts of both the single- and multi-photon selections were sufficiently loose so that no further optimization was found to be necessary. However, I developed

---

[9] These predictions were obtained using the `KKMC` generator, assuming Standard Model couplings of electrons and neutrinos. At LEP2 energies, the W-related contributions were expected to be dominated by the W amplitude squared: $\sigma_{WZ}/\sigma_W \simeq 0.3$.

a special selection to search for events with photons not originating from the beam vertex, the "non-pointing" photons. In all cases the dominant background came from the Standard Model process $e^+e^- \rightarrow \nu\bar{\nu}\gamma(\gamma)$, which has been studied in the beginning of this chapter.

The selection efficiency for the signal was estimated using large samples of Monte Carlo events simulated using the `SUSYGEN` Monte Carlo generator [66]. The signal efficiency was defined as the number of selected signal events divided by the the total number of generated events. For each signal mass point about 5,000 MC events were produced. Unless otherwise stated, no phase space cuts were applied during the generation of signal Monte Carlo samples. All generated events were passed through the L3 detector simulation program as described in Section 4.2.10 of Chapter 4.

The rest of this section is organized as follows. In the next section, I describe the statistical procedure that I used to quantify the results of my searches. Single-photon and multi-photon signatures are investigated in Sections 7.2.2 and 7.2.3, respectively. Section 7.2.4 is devoted to searches for events with non-pointing photons.

7.2.1 Calculating Limits on New Physics

The observed event rates and kinematic distributions were found to be in good agreement with the Standard Model expectations (see Sections 6.3.8 and 6.4). In the absence of a clear evidence for the signal, the goal of a search is to place the most stringent possible limits on the signal cross section which can then be used to constrain the parameters of the underlying theory. Below I describe the statistical procedure that I used for calculating such limits on new physics.

The first step of this procedure consists of constructing the likelihood as a function of the number of expected signal events. To determine the likelihood function, one needs to choose a distribution discriminating the new physics signal from the Standard Model background. For searches in the single-photon channel, I used the two dimensional distribution M_{rec} *vs.* $|\cos\theta_\gamma|$ which fully described the kinematics of the selected single-photon events. In the multi-photon channel, I used the distribution of the final discriminant variable computed from the reconstructed recoil mass and the measured photon energies and polar angles as described in Section 7.2.3.

The likelihood function is defined as a product of Poisson probabilities of observing n_i data events in bin i of the discriminating distribution:

$$\mathcal{L}(s) = \prod_{i=1}^{n_{bin}} \frac{\mathrm{e}^{-(s_i+b_i)}(s_i+b_i)^{n_i}}{n_i!}, \qquad (7.10)$$

where n_{bin} is the total number of bins, s_i and b_i are the numbers of expected signal and background events, respectively, and $s = \sum_i s_i$ is the total number of expected signal events. Since the signal cross section usually increases with the center-of-mass energy, the likelihood functions are computed separately for each $\sqrt{s}$. The combined likelihood function is then obtained by multiplying together the individual likelihoods:

$$\mathcal{L}(s) = \prod_{k=1}^{n_{sample}} \mathcal{L}(s_k), \qquad (7.11)$$

where $n_{sample} = 8$ is the number of energy points considered in my analysis (see Table 6.1 p. 132) and $s = \sum_k s_k$ is the total expected signal. The likelihood method uses information from both the total event rate and the shape of the discriminating distribution. Thus, no further optimization of the event selection is necessary, in contrast to the event-counting method where further cuts on the discriminating variables are typically required to improve the sensitivity of the search.

The next step of the statistical procedure consists of constructing the estimator *(test-statistic)* which can be used to evaluate the compatibility of the data with the predicted signal. There exist several choices of test-statistic. I used the test-static given by the normalized integral of the likelihood function [188]:[10]

$$X(s) = \frac{\int_s^\infty \mathcal{L}(x)dx}{\int_0^\infty \mathcal{L}(x)dx}, \qquad (7.12)$$

---

[10] In L3, this test-statistic has been used to set limits on the mass of the Standard Model Higgs boson [189]. Another popular choice is the likelihood ratio $X(s) = \mathcal{L}(s)/\mathcal{L}(0)$, which has been adopted for the combination of LEP results on searches for Higgs bosons [11]. Extensive studies have shown that these two estimators provide similar sensitivity to signal [190]. As a cross check, I repeated my analysis using the likelihood-ratio method and found no noticeable changes in the observed or expected limits on new physics.

which can be interpreted as the Bayesian confidence level assuming a uniform prior distribution. A high value of $X(s)$ indicates that the observed data agrees better with the signal+background hypothesis, while a low value favors the background-only hypothesis. This property of the test-statistic is then used to derive limits on the signal cross section.

First, the value of test-statistic X_{obs}, measured in data, is compared to the test-statistic distribution obtained from a large number of reference Monte Carlo samples (N_{MC}). Each Monte Carlo sample corresponds to a possible outcome of a real experiment in the presence of both the signal and the background. The fraction of outcomes with the test statistic value less than that of the data ($X_{s+b} < X_{\text{obs}}$) gives the confidence level for the signal+background hypothesis:

$$\text{CL}_{s+b}(s) \;=\; \frac{N_{X_{s+b}<X_{\text{obs}}}}{N_{\text{MC}}}\,. \tag{7.13}$$

Similarly, the confidence level for the background-only hypothesis $\text{CL}_b(s)$ is computed using Monte Carlo experiments generated assuming the absence of a signal.

The frequentist exclusion limit is usually computed from the confidence $\text{CL}_{s+b}(s)$. The signal hypothesis is considered to be excluded at the 95% confidence level if an observation is made such that $\text{CL}_{s+b}(s)$ is less than 0.05. However, this procedure may lead to the following undesired possibility: a large downward fluctuation in data would allow to exclude hypotheses for which the experiment should have no sensitivity. This problem can be avoided by introducing the ratio $\text{CL}_s = \text{CL}_{s+b}/\text{CL}_b$ [191]. The signal hypothesis is considered to be excluded at the 95% confidence level (C.L.) if the corresponding confidence CL_s satisfies

$$1 - \text{CL}_s(s) \geq 0.95\,. \tag{7.14}$$

The 95% C.L. upper limit on the total number of signal events is then derived by finding the minimum value of s which still satisfies the above condition.

As mentioned above, the L3 data used in my searches for new physics were recorded at eight different center-of-mass energies ranging from 189 GeV to 208 GeV. Therefore, the upper limit on the signal cross section at a reference center-of-mass energy ($\sqrt{s}_0$) can be calculated as

$$\sigma_s^{95}(\sqrt{s}_0) = \frac{s_{95}}{\sum\limits_{k=1}^{8} \mathcal{L}_k \, \varepsilon_k \, \dfrac{\sigma_s(\sqrt{s}_k)}{\sigma_s(\sqrt{s}_0)}} \,, \tag{7.15}$$

where s_{95} is the 95% C.L. upper limit on the total number of signal events and $\sigma_s(\sqrt{s})$ is the signal cross section as a function of $\sqrt{s}$. The summation is performed over the eight energy points $\sqrt{s}_k$ with $\mathcal{L}_k$ and ε_k being the integrated luminosity and the selection efficiency for signal events, respectively. The reference energy point is chosen to be $\sqrt{s}_0 = 207$ GeV, which approximately corresponds to the highest center-of-mass energy reached at LEP.

Systematic errors on the signal and background expectations can be conveniently taken into account during the generation of Monte Carlo experiments [191]. In each trial experiment, candidates are generated according to the signal and background distributions which are smeared to account for systematic errors on the selection efficiency, integrated luminosity, and predicted cross sections of the background processes. The smearing is performed using a set of Gaussian distributions with standard deviations equal to the individual systematic uncertainties [191]. In my analysis, the relative systematic uncertainties were at a level of 1% (see Table 7.2), and their effects on the obtained limits were found to be negligible.[11]

The Monte Carlo method can also be used to estimate the exclusion power of a search. This is usually done by computing the expected upper limit on the signal cross section, defined as the median limit from an ensemble of the Monte Carlo experiments generated assuming the absence of a signal.

---

[11] As a cross check, I also evaluated the systematic effects using the method of Cousins and Highland [192]. The two estimates were found to agree with each other.

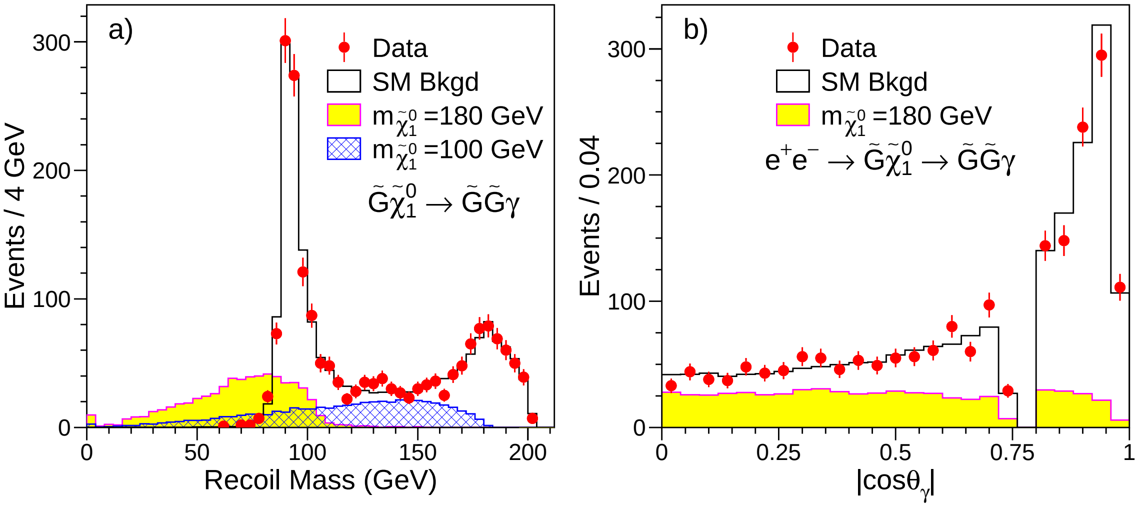

Figure 7.5: a) Recoil mass spectra and b) polar angle distributions of the fully simulated $e^+e^- \rightarrow \tilde\chi^0_1\tilde{G} \rightarrow \tilde{G}\tilde{G}\gamma$ Monte Carlo events that were accepted by the single-photon selection for the mass hypotheses $m_{\tilde\chi^0_1} = 100$ and 180 GeV. Also shown are the corresponding distributions for the data and background. The normalization for the signal Monte Carlo is arbitrary.

7.2.2 Single-Photon Signatures

$e^+e^- \rightarrow \tilde\chi^0_1\tilde{G} \rightarrow \tilde{G}\tilde{G}\gamma$

As discussed in Section 3.2.4, in no-scale supergravity models the gravitino can become "superlight" (10^{-6} eV $\lesssim m_{\tilde{G}} \lesssim 10^{-4}$ eV), leading to a sizable cross section for the reaction $e^+e^- \rightarrow \tilde{G}\tilde\chi^0_1$. Since the dominant decay mode is expected to be $\tilde\chi^0_1 \rightarrow \tilde{G}\gamma$, this process would lead to events with a single photon and missing energy in the final state.

Signal efficiencies for this process were found to range between 75% at the kinematic limit and 69% for $m_{\tilde\chi^0_1} = 5$ GeV. The kinematically allowed range of the photon recoil mass depends on the neutralino mass and is given by

$$0 < M_{\rm rec} < \sqrt{s - m_{\tilde\chi^0_1}}\,. \tag{7.16}$$

Figure 7.5a compares the recoil mass spectrum of the signal events accepted by the single-photon selection with those of the data and the Standard Model background.

Because the $\nu\bar{\nu}\gamma$ background peaked at $M_{\rm rec} \simeq M_Z$, the region of the highest sensitivity corresponded to $M_{\rm rec} \lesssim 80$ GeV. No excess over the Standard Model expectation was observed. In particular, in the region of interest, $M_{\rm rec} < 70$ GeV, 2 events were found in data with 3.8 ± 0.8 events expected from background. It should be noted that the RFQ calibration (see Chapter 5) played an important role in improving the sensitivity of this search. For comparison, with calibrations used during 1989-1996 the number of background events in the region $M_{\rm rec} < 70$ GeV would have been 3-4 times higher.

Figure 7.5b shows that the $|\cos\theta_\gamma|$ distribution of the signal events was almost flat. Therefore, this distribution could also be used to discriminate the signal from the $\nu\bar{\nu}\gamma$ background. To derive upper limits on the signal cross section, I performed a fit to the two-dimensional distribution $M_{\rm rec}$ *vs.* $|\cos\theta_\gamma|$. Figure 7.6a shows the observed and expected 95% C.L. limits derived at $\sqrt{s} = 207$ GeV. Data collected at lower $\sqrt{s}$ were included assuming the signal cross section to scale as β^8/s with $\beta = \sqrt{1 - m^2_{\tilde{\chi}^0_1}/s}$ [193].

In the LNZ model, there are only two free parameters – the gravitino and the neutralino masses (see Section 3.2.4). Thus, the obtained cross section limits could be translated into an excluded region in the $(m_{\tilde{\chi}^0_1}, m_{\tilde{\rm G}})$ mass plane as shown in Figure 7.6b. Gravitino masses below 10^{-5} eV were excluded for neutralino masses below 175 GeV.

$e^+e^- \to$ XY with X $\to$ Yγ

The selected single-photon events were also used to search for evidence of new physics processes of type $e^+e^- \to XY \to YY\gamma$, where X and Y were new neutral undetectable particles[12] and the X $\to$ Yγ decay was assumed to occur with a 100% branching ratio. For many SUSY processes, including the reaction $e^+e^- \to \tilde{\chi}^0_1\tilde{\rm G} \to \tilde{\rm G}\tilde{\rm G}\gamma$ considered above and the reaction $e^+e^- \to \tilde{\chi}^0_2\tilde{\chi}^0_1 \to \tilde{\chi}^0_1\tilde{\chi}^0_1\gamma$ described in Section 3.2.3, the distributions for the production and decay angles were expected to be approximately

---

[12] Such searches are often called model-independent because no further assumptions on the nature of these new particles are made.

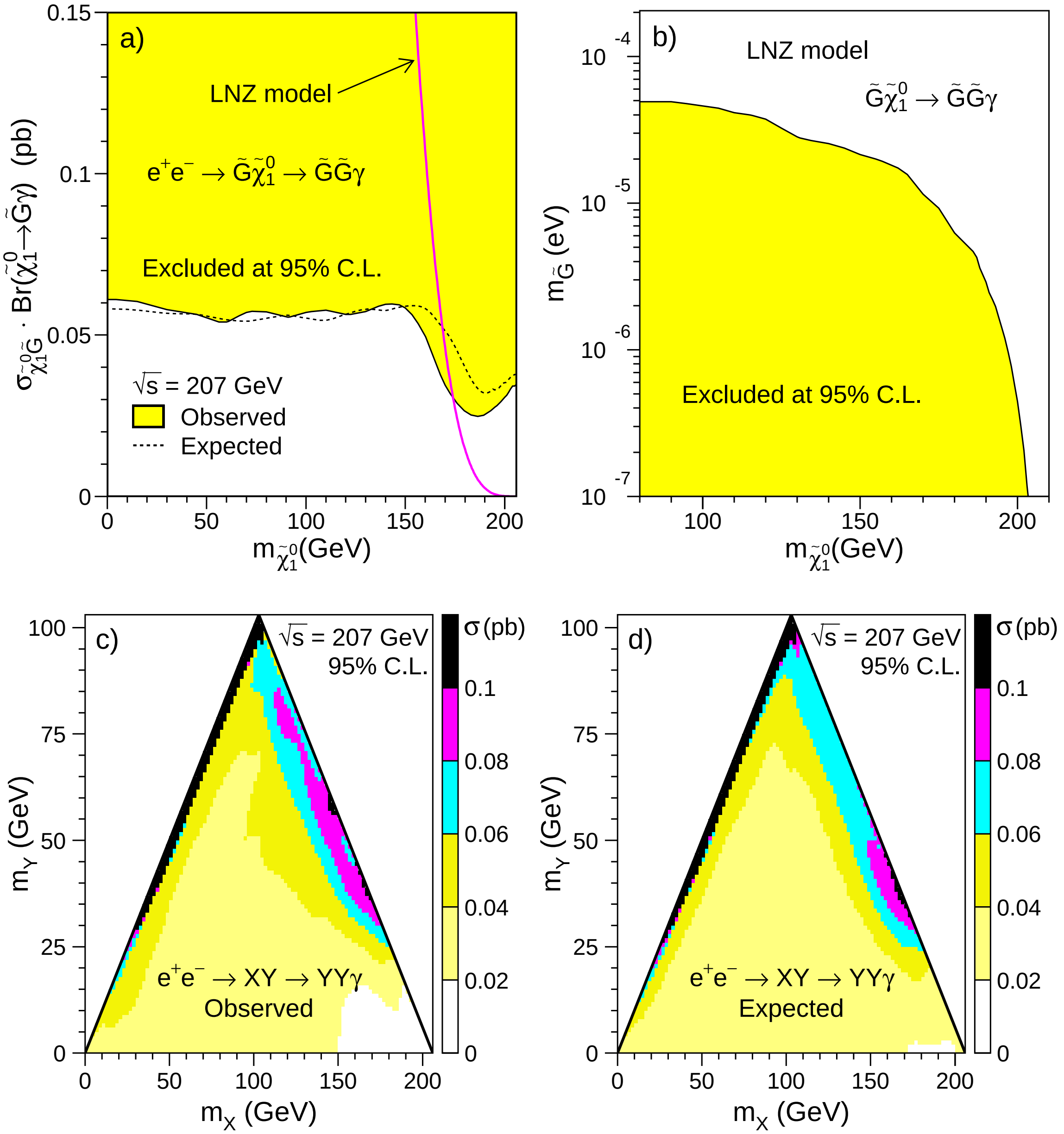

Figure 7.6: **a)** Observed and expected 95% confidence level upper limits on the production cross section of the reaction $e^+e^- \to \tilde{G}\tilde{\chi}_1^0 \to \tilde{G}\tilde{G}\gamma$. The cross section predicted by the LNZ model [193] for $m_{\tilde{G}} = 10^{-5}$ eV is also shown. Data collected at lower $\sqrt{s}$ were included assuming the signal cross section to scale as β^8/s. **b)** Region excluded for the LNZ model in the $(m_{\tilde{\chi}_1^0}, m_{\tilde{G}})$ mass plane. **c)** Observed and **d)** expected cross section upper limits from the search for a generic process $e^+e^- \to XY$ with $X \to Y\gamma$. The limits were obtained at the 95% C.L. for $\sqrt{s}$ = 207 GeV. Data collected at lower $\sqrt{s}$ were included assuming the signal cross section to scale as β_0/s, where β_0 is defined in the text.

isotropic. I therefore also performed this search under the assumption of isotropically distributed production and decay angles. This resulted in a substantial increase in experimental sensitivity because not only the total number of observed events but also the angular and recoil mass distributions could be used to differentiate the signal from the $e^+e^- \to \nu\bar{\nu}\gamma$ background.

No significant deviation from the Standard Model expectations was observed, and cross section limits were derived for all allowed values of the masses m_X and m_Y in steps of 3 GeV. The limits were obtained at $\sqrt{s} = 207$ GeV, and data collected at lower $\sqrt{s}$ were included assuming the signal cross section to scale[13] as β_0/s, where $\beta_0 = \sqrt{1 - 2(x_1 + x_2) + (x_1 - x_2)^2}$ with $x_1 = m_X^2/s$ and $x_2 = m_Y^2/s$.

Figures 7.6c,d show that the obtained limits were in good agreement with the expectation. For most of the kinematically allowed values of m_X and m_Y, the obtained cross section limits were in the range of 0.02-0.05 pb.

Comparable cross section limits were also obtained for the special case of the reaction $e^+e^- \to \tilde{\chi}_2^0\tilde{\chi}_1^0 \to \tilde{\chi}_1^0\tilde{\chi}_1^0\gamma$. The LEP combined search for this process will be discussed in Appendix E.

$\mathbf{e^+e^- \to \widetilde{G}\widetilde{G}\gamma}$

Models with superlight gravitinos may also lead to pair-production of gravitinos accompanied by a photon from initial-state radiation, $e^+e^- \to \tilde{G}\tilde{G}\gamma$, giving rise to a single-photon and missing energy signature. Even if the masses of all other SUSY particles were above $\sqrt{s}$, this process could still provide a means to detect Supersymmetry at LEP.

As discussed in Section 3.2.4 (p. 51), the photon energy spectrum was expected to be soft. Therefore, for this search I considered only events from the combined single- and soft-photon sample with $x_\gamma < 0.5$, where $x_\gamma = E_\gamma/E_{beam}$. In total, I selected 1,286 such events in data with 1,303.6 events expected from Standard Model processes. The corresponding distributions of the photon energy and polar angle are

---

[13] Since the energy spread at LEP2 was relatively small, I assumed that a possible dependence of the matrix element on $\sqrt{s}$ was negligible.

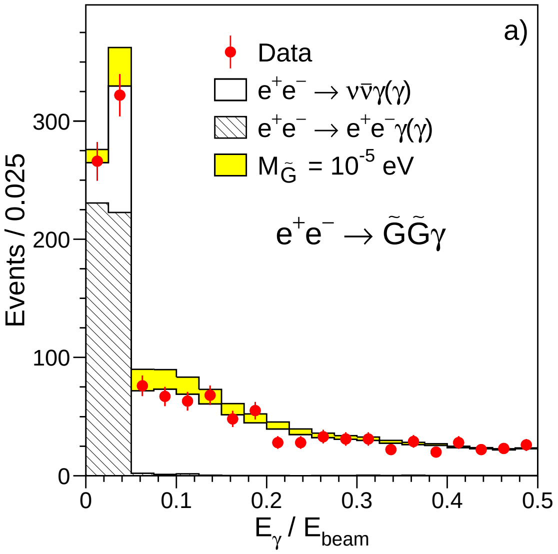

Figure 7.7: Distributions of a) the ratio of the photon energy to the beam energy (x_γ) and b) the photon polar angle for events with $x_\gamma < 0.5$ from the combined single- and soft-photon sample. Signal expected from the reaction $\mathrm{e}^+\mathrm{e}^- \to \tilde{\mathrm{G}}\tilde{\mathrm{G}}\gamma$ is also shown for $m_{\tilde{\mathrm{G}}} = 10^{-5}$ eV.

shown in Figure 7.7. The predictions for the signal were obtained using a sample of 40,000 fully simulated Monte Carlo events. The signal efficiency within the above kinematic acceptance region was estimated to be 62%.

The inclusion of the soft-photon sample resulted in a significant increase in the accepted signal cross section. The achieved improvement in the search sensitivity was equivalent to increasing the integrated luminosity by approximately 50%.

In order to place an upper limit on the signal cross section, I performed a two-dimensional fit to the x_γ *vs.* $|\cos\theta_\gamma|$ distribution. As the signal cross section was proportional to $1/m^4_{\tilde{\mathrm{G}}}$, this limit could be translated into a lower limit on the gravitino mass:

$$m_{\tilde{\mathrm{G}}} > 1.35 \times 10^{-5}\ \mathrm{eV},$$

at the 95% confidence level, which in turn corresponded to a lower limit on the SUSY breaking scale $\sqrt{F} > 238$ GeV. The expected lower limit on the gravitino mass was estimated to be 1.32×10^{-5} eV.

7.2.3 Multi-Photon Signatures

Neutralino Production in GMSB

In models with gauge-mediated SUSY breaking (GMSB), the lightest supersymmetric particle (LSP) is always a light gravitino, 10^{-2} eV $\lesssim m_{\tilde{\mathrm{G}}} \lesssim 10^{2}$ eV. If the next-to-lightest supersymmetric particle (NLSP) is the lightest neutralino, it is expected to decay predominantly through $\tilde{\chi}^0_1 \to \tilde{\mathrm{G}}\gamma$. In this scenario pair-production of the lightest neutralinos, $\mathrm{e}^+\mathrm{e}^- \to \tilde{\chi}^0_1\tilde{\chi}^0_1$, would lead to a multi-photon plus missing energy signature. A detailed description of this SUSY process was provided in Section 3.2.1.

In order to differentiate the signal from the $\mathrm{e}^+\mathrm{e}^- \to \nu\bar{\nu}\gamma\gamma$ background, I used the following five kinematic variables: the energies of the two most energetic photons, their polar angles, and the recoil mass to the multi-photon system. Figure 7.8 compares the corresponding distributions of the signal for $m_{\tilde{\chi}^0_1} = 90$ GeV[14] with those of the data and the Standard Model background for events accepted by the multi-photon selection (see Section 6.4). All measured distributions were found to agree with the Standard Model predictions. In particular, no candidates with $E_{\gamma_2}/E_{beam} > 0.45$ or $M_{\mathrm{rec}} < 75$ GeV were found in the data. As shown in Figure 7.8, the observation of such events would have been a clear indication of the signal.

To combine information from these kinematic variables, I used the following procedure. First, I computed probability distributions for each of the five input variables, separately for each signal mass hypothesis and the Standard Model background. These probability distributions were then combined in a final discriminant variable.

Let us take s_i and b_i to be the probability distributions for variable i for a given signal hypothesis and the background, respectively. For a single variable, the probability for an event to belong to signal is then given by

$$p_i(x_i) = \frac{s_i(x_i)}{s_i(x_i) + b_i(x_i)}\,, \tag{7.17}$$

---

[14] The signal distributions were obtained from a large sample of Monte Carlo events processed through the full detector simulation. Similar distributions for other values of the neutralino mass can be found in Figure 3.8 (p. 45).

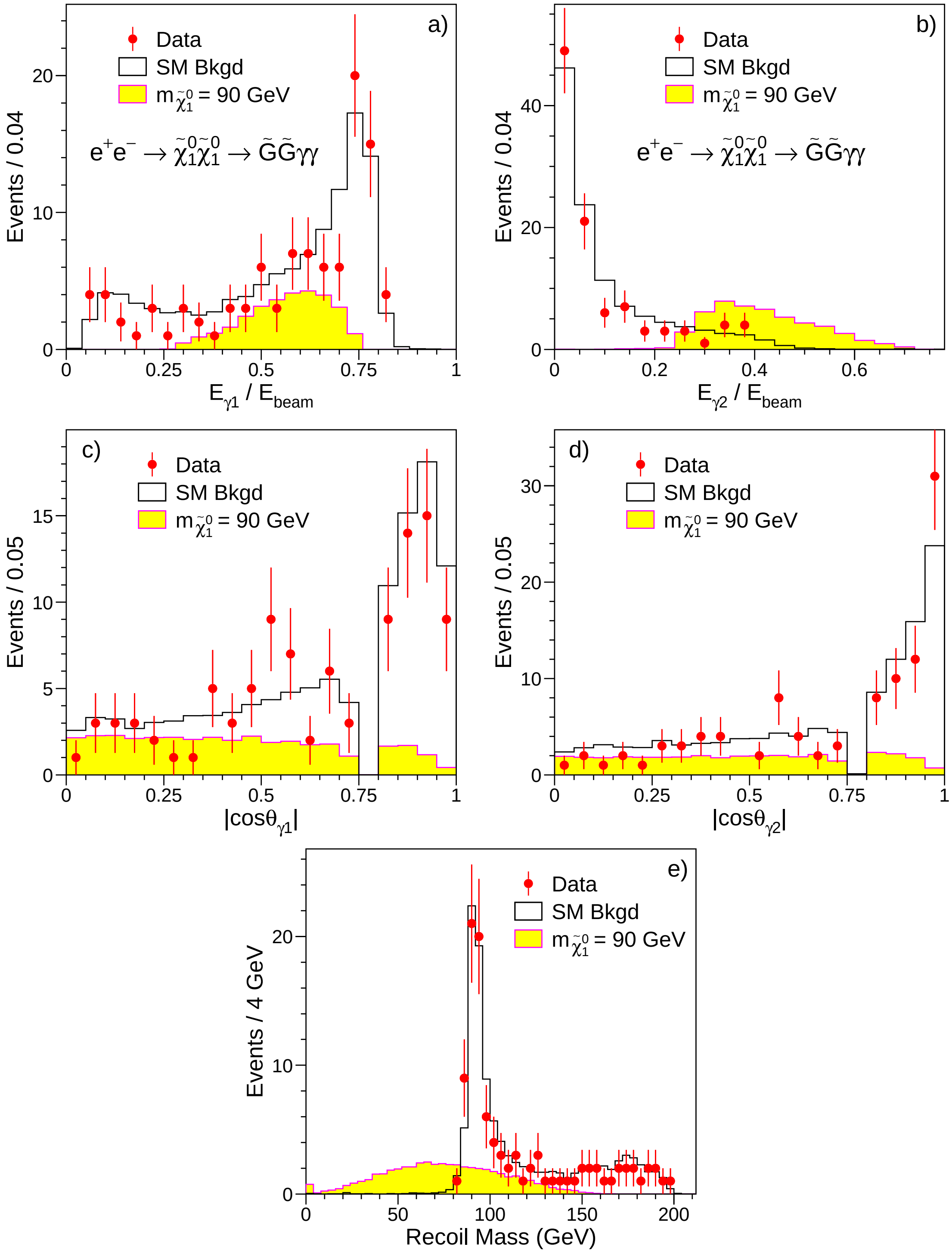

Figure 7.8: Distributions of (a,b) the photon energies and (c,d) the photon polar angles and e) the recoil mass spectrum of the fully simulated $e^+e^- \rightarrow \tilde{\chi}_1^0\tilde{\chi}_1^0 \rightarrow \tilde{G}\tilde{G}\gamma\gamma$ Monte Carlo events that were accepted by the multi-photon selection for $m_{\tilde{\chi}_1^0} = 90$ GeV. Also shown are the corresponding distributions for the data and the Standard Model background. The normalization for the signal Monte Carlo is arbitrary.

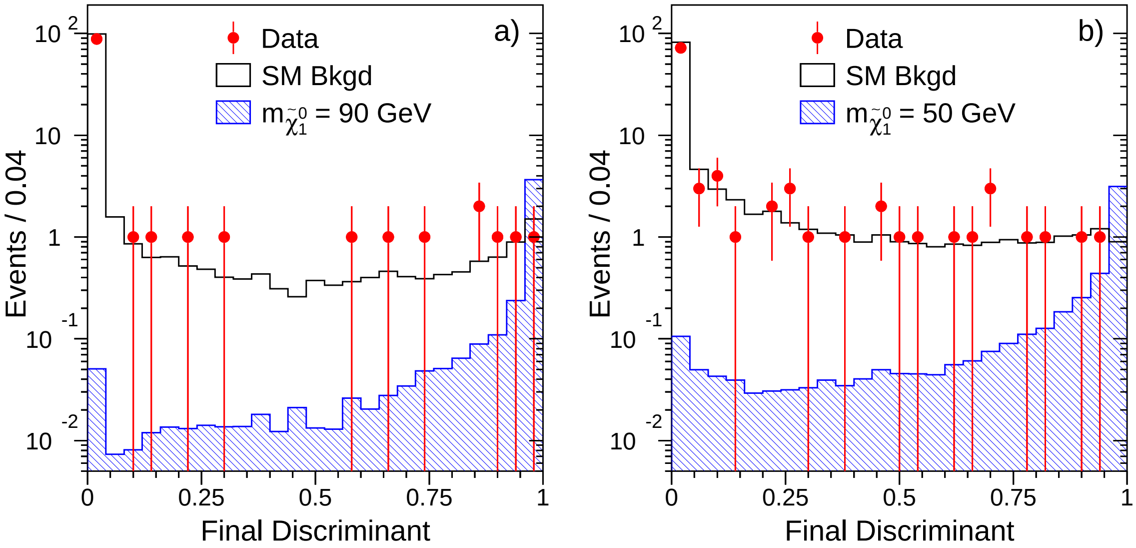

Figure 7.9: Distributions of the final discriminant variable used in the search for pair-produced neutralinos $\tilde{\chi}_1^0\tilde{\chi}_1^0 \to \tilde{G}\tilde{G}\gamma\gamma$ a) for $m_{\tilde{\chi}_1^0} = 90$ GeV and b) for $m_{\tilde{\chi}_1^0} = 50$ GeV. The signals correspond to the upper limits of a) 4.7 and b) 5.2 events derived for these mass points.

where x_i is the value of this variable measured for this event. Similarly, the probability that this event belongs to the background is given by

$$q_i(x_i) = \frac{b_i(x_i)}{s_i(x_i) + b_i(x_i)} \,. \tag{7.18}$$

The final discriminant variable is then computed by multiplying the individual probabilities from each of the five input variables:

$$F(\vec{x}) = \frac{\prod_{i=1}^{5} p_i(x_i)}{\prod_{i=1}^{5} p_i(x_i) + \prod_{i=1}^{5} q_i(x_i)} \,. \tag{7.19}$$

For a more signal-like event, F would be close to one, while for a very background-like event, $F \to 0$.

Figure 7.9 shows the distributions of the final discriminant variable for two neutralino mass hypotheses: $m_{\tilde{\chi}_1^0} = 90$ GeV and $m_{\tilde{\chi}_1^0} = 50$ GeV. In both cases, the signal was almost completely separated from the background and no excess in the signal region $F \gtrsim 0.9$ was observed in the data. The same held for other mass points.

Upper limits on the signal cross section were derived from fits to the obtained final discriminant distributions. The signal efficiency for this process was found to decrease from 70% for $m_{\tilde{\chi}^0_1} \simeq 100$ GeV to 40% for $m_{\tilde{\chi}^0_1} = 5$ GeV. The observed and expected limits derived at $\sqrt{s} = 207$ GeV are shown in Figure 7.10a as a function of the neutralino mass. Data collected at lower $\sqrt{s}$ were included assuming the signal cross section to scale according to the MGM model [194]. In this model, the neutralino is pure bino and the masses of scalar electrons are related to the neutralino mass through $m_{\tilde{\mathrm{e}}_\mathrm{L}} = 1.1 \times m_{\tilde{\chi}^0_1}$ and $m_{\tilde{\mathrm{e}}_\mathrm{R}} = 2.5 \times m_{\tilde{\chi}^0_1}$. The signal cross section predicted by the MGM model is also shown in Figure 7.10a. The neutralino mass limit obtained for this model was

$$m_{\tilde{\chi}^0_1} > 99.5 \text{ GeV}$$

at the 95% confidence level. Figure 7.10b shows the excluded region in the $(m_{\tilde{\mathrm{e}}_\mathrm{R}}, m_{\tilde{\chi}^0_1})$ mass plane obtained after relaxing the mass relations of the MGM. Also shown is the region suggested by the interpretation [68] of the rare CDF event in the scalar electron scenario (see Section 3.2.2). This interpretation was ruled out by my analysis.

The multi-photon selection used in this search was devised for photons originating from the interaction point, and the above limits were derived under the assumption of a neutralino mean decay length shorter than about 5 cm. In the next section I will describe a dedicated analysis that I developed for the special case of a non-negligible neutralino lifetime.

Neutralino Production in SUGRA Models

In gravity-mediated SUSY breaking models (SUGRA) the lightest neutralino is expected to be the LSP. This scenario may lead to a new source of multi-photon events from the reaction $\mathrm{e}^+\mathrm{e}^- \to \tilde{\chi}^0_2\tilde{\chi}^0_2$ followed by the decay $\tilde{\chi}^0_2 \to \tilde{\chi}^0_1\gamma$ as described in Section 3.2.3. The signal kinematic distributions were expected to very similar to those from the GMSB reaction $\mathrm{e}^+\mathrm{e}^- \to \tilde{\chi}^0_1\tilde{\chi}^0_1$ considered above. Therefore the same analysis procedure was used.

No significant deviation from the Standard Model expectations was observed and

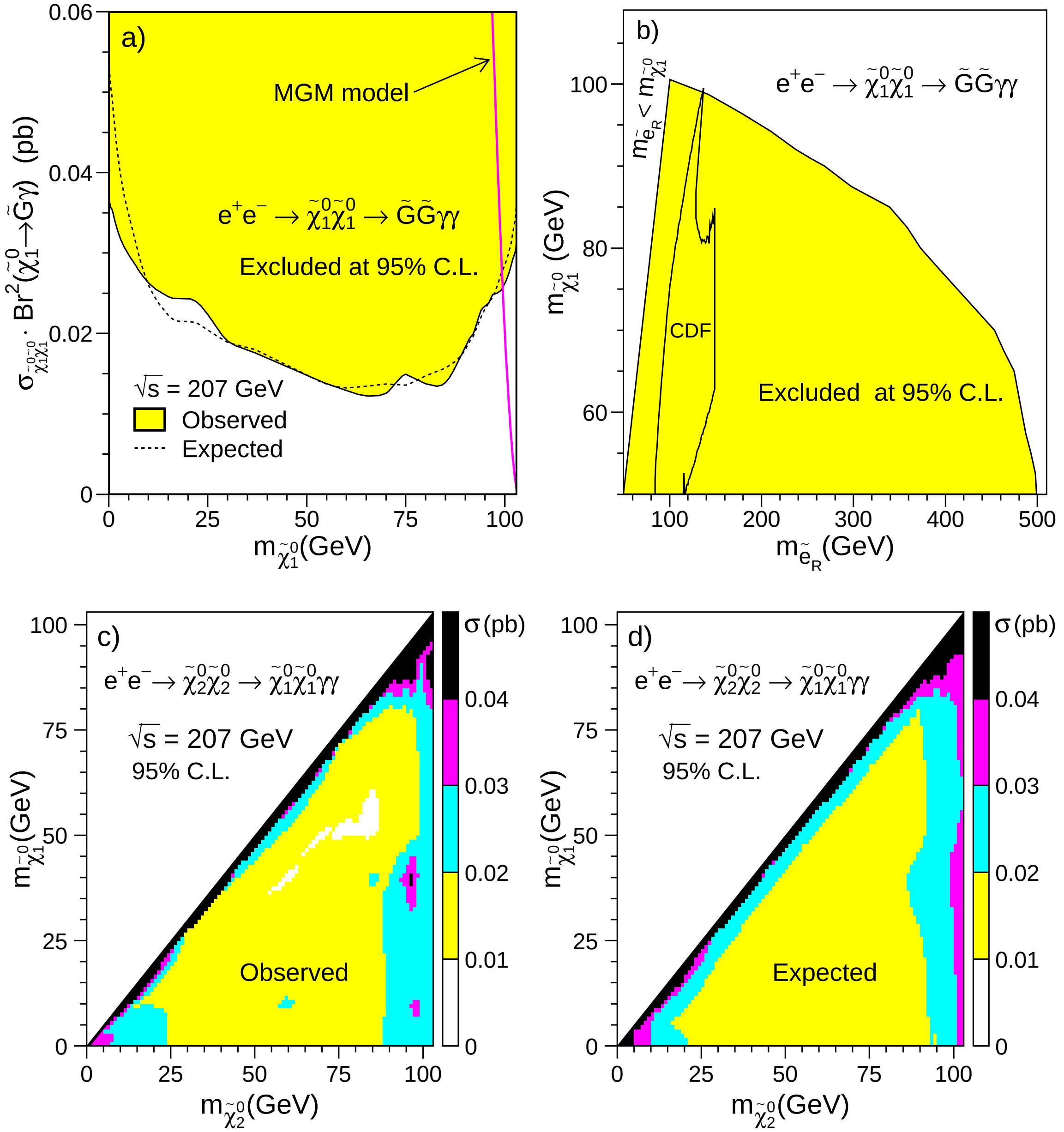

Figure 7.10: **a)** Observed and expected 95% confidence level upper limits on the production cross section of the reaction $e^+e^- \to \tilde\chi_1^0\tilde\chi_1^0 \to \tilde G\tilde G\gamma\gamma$. The cross section predicted by the MGM model [194] is also shown. **b)** Region excluded for a pure bino neutralino model in the $(m_{\tilde e_R}, m_{\tilde\chi_1^0})$ mass plane. The region compatible with the GMSB interpretation of the CDF event [68] is also shown. **c)** Observed and **d)** expected cross section upper limits from the search for the process $e^+e^- \to \tilde\chi_2^0\tilde\chi_2^0 \to \tilde\chi_1^0\tilde\chi_1^0\gamma\gamma$. The limits were obtained at the 95% C.L. for $\sqrt{s} = 207$ GeV. Data collected at lower $\sqrt{s}$ were included assuming the signal cross section to scale according to Equation 3.22 (p. 49). For simplicity, the branching fraction for the $\tilde\chi_2^0 \to \tilde\chi_1^0\gamma$ decay was assumed to be 100%.

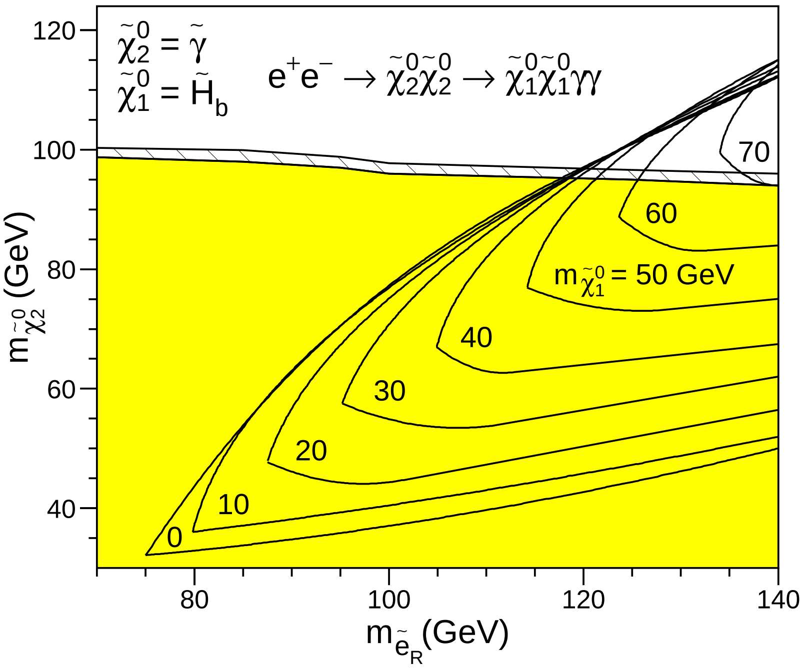

Figure 7.11: Region excluded at the 95% confidence level in the $(m_{\tilde{e}_R}, m_{\tilde{\chi}_2^0})$ mass plane. The shaded region corresponds to $m_{\tilde{e}_L} \gg m_{\tilde{e}_R}$ and the hatched region is additionally excluded when $m_{\tilde{e}_L} = m_{\tilde{e}_R}$. The mass difference between $\tilde{\chi}_2^0$ and $\tilde{\chi}_1^0$ was assumed to be greater than 10 GeV. The regions kinematically allowed for the CDF event [69] as a function of $m_{\tilde{\chi}_1^0}$ are also indicated.

cross section limits were derived for all kinematically allowed values of neutralino masses in steps of 3 GeV. The limits were obtained at $\sqrt{s}$ = 207 GeV, and data collected at lower $\sqrt{s}$ were included assuming the signal cross section to scale according to Equation 3.22 (p. 49). The observed and expected limits are shown in Figures 7.10c,d. For most of the kinematically allowed values of $m_{\tilde{\chi}_1^0}$ and $m_{\tilde{\chi}_2^0}$, the obtained cross section limits were in the range of 0.01-0.03 pb.

The $\tilde{\chi}_2^0 \to \tilde{\chi}_1^0\gamma$ decay has a branching fraction close to 100% if one of the two neutralinos is pure photino and the other pure higgsino. This scenario is suggested by the SUGRA interpretation of the $ee\gamma\gamma$ event observed by CDF (see Section 3.2.2). With this assumption, a lower limit on the $\tilde{\chi}_2^0$ mass was calculated as a function of $m_{\tilde{e}_R}$ using the most conservative cross section upper limit for any mass difference between $\tilde{\chi}_2^0$ and $\tilde{\chi}_1^0$ greater than 10 GeV. Figure 7.11 shows the regions of the $(m_{\tilde{\chi}_2^0}, m_{\tilde{e}_R})$ plane excluded at the 95% C.L. Two distinct scenarios were investigated: $m_{\tilde{e}_L} = m_{\tilde{e}_R}$ and

$m_{\tilde{e}_L} \gg m_{\tilde{e}_R}$, where $m_{\tilde{e}_L}$ and $m_{\tilde{e}_R}$ denote the masses of the left- and right-handed scalar electrons. The regions kinematically allowed for the SUGRA interpretation of the CDF event [69] are also indicated.

7.2.4 Searches for Events with Non-Pointing Photons

As discussed in Section 3.2 of Chapter 3, the neutralino in GMSB models can have a non-negligible lifetime. The neutralino decay length is proportional to the gravitino mass squared (see Equation 3.21 p. 45) and, for $m_{\tilde{G}} \sim 100$ eV, it can be comparable to or even larger than the size of the L3 detector. In this scenario, one or both of the neutralinos produced in the reaction $e^+e^- \rightarrow \tilde{\chi}^0_1\tilde{\chi}^0_1 \rightarrow \tilde{G}\tilde{G}\gamma\gamma$ may decay within the sensitive volume of the detector, but at a distance from the primary vertex. This results in a topology with sizable missing energy carried away by the gravitinos and with one or two visible energetic photons which, in general, do not point back to the interaction region. The single-photon topology can be produced if one of the neutralinos decays outside the active detector region.

In this section I describe a dedicated analysis that I developed to search for such events with non-pointing photons and missing energy. To improve the sensitivity, I searched for non-pointing photons not only in the BGO but also in the hadron calorimeter of L3. This was important because for this search the compactness of the BGO crystal calorimeter presented a disadvantage.

Figure 7.12 shows a simulated $e^+e^- \rightarrow \tilde{\chi}^0_1\tilde{\chi}^0_1 \rightarrow \tilde{G}\tilde{G}\gamma\gamma$ event with two non-pointing photons. In this event one of the neutralinos decayed in front of the BGO calorimeter, giving rise to an electromagnetic shower in the BGO crystals, while the other decayed and produced a shower inside the hadron calorimeter. This example suggests a study of the following event signatures:

- Events with one or two non-pointing photons in the BGO.
- Events with one or two non-pointing photons in the HCAL.
- Events with photon candidates in both the BGO and the HCAL.

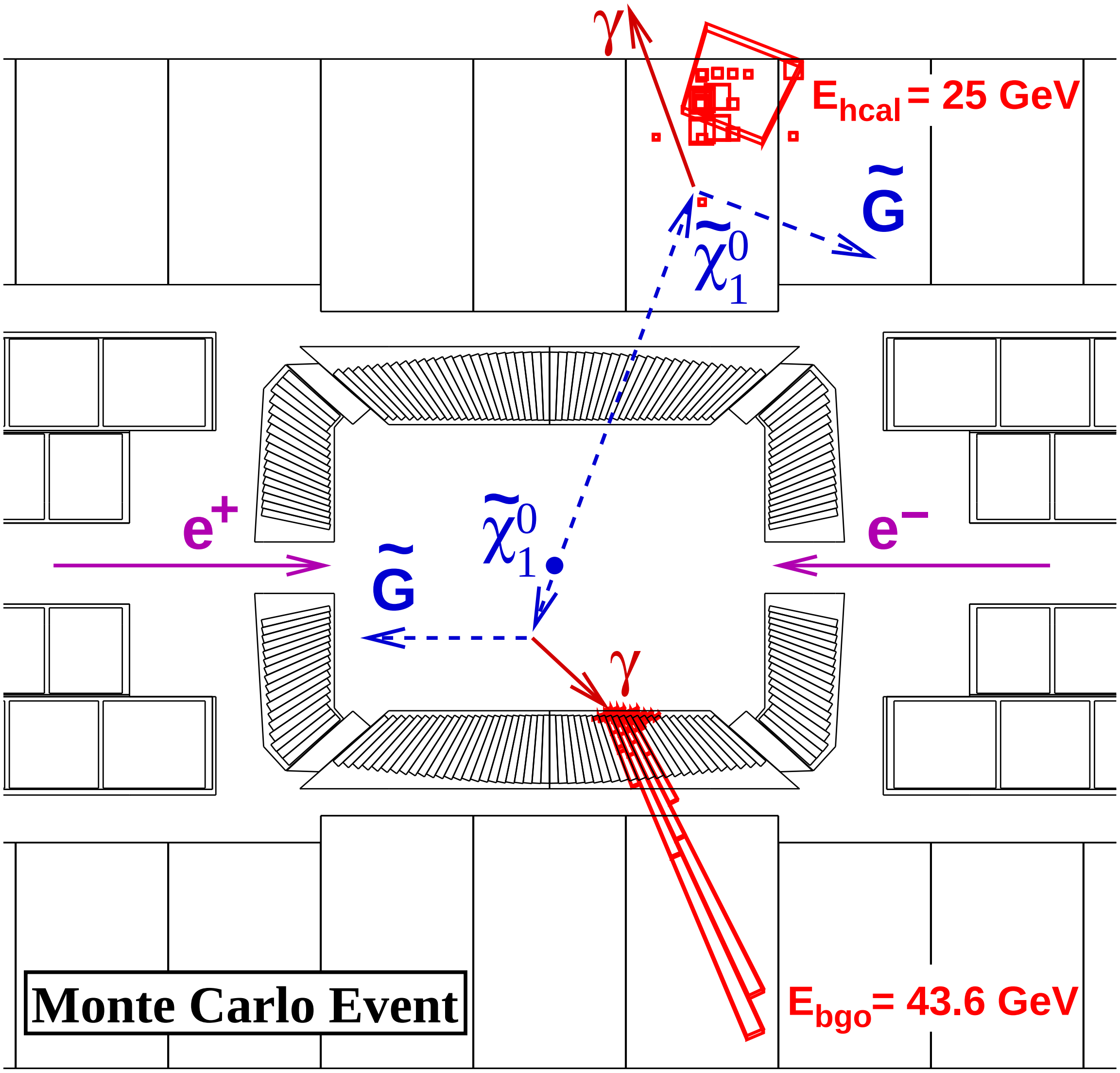

Figure 7.12: Schematic diagram of a simulated $e^+e^- \to \tilde{\chi}_1^0\tilde{\chi}_1^0 \to \tilde{G}\tilde{G}\gamma\gamma$ event with non-pointing photons. The event is displayed in a plane parallel to the beam axis. The arrows indicate the directions of flight of the produced particles. One of the two neutralinos decayed in front of the BGO calorimeter after traveling a distance of 0.3 m, and the other decayed in the HCAL after traveling 1.6 m. This event was taken from a Monte Carlo sample generated with $m_{\tilde{\chi}_1^0} = 95$ GeV and $\sqrt{s} = 207$ GeV and processed through the full detector simulation. Energy deposits in the BGO are shown as towers whose height is proportional to the crystal energy. Hits in the HCAL are shown as squares whose size is proportional to the deposited energy. The reconstructed shower energies are also indicated.

Non-pointing Photons in the BGO

Contrary to photons produced near the interaction region, non-pointing photons were expected to enter the BGO calorimeter at a significant angle with respect to the crystal axis (see Figure 7.12). As a consequence, electromagnetic showers produced by non-pointing photons could be identified by studying the transverse shower profile. In particular, a measure of shower's transverse circularity was provided by the variable *shower roundness* (see Equation 6.2 p. 140). For photons produced near the primary vertex, the transverse shower profile was almost circular so that their roundness was typically close to one. In contrast, showers produced by non-pointing photons were expected to be oblong, which would result in lower values of shower roundness.

For this event signature I applied the same basic event selection criteria as those used in the selection of single- and multi-photon events from the process $e^+e^- \to \nu\bar{\nu}\gamma(\gamma)$ (see Sections 6.3 and 6.4), except that I did not apply the cuts based on the measured lateral shower profile.[15] Instead I required that at least one photon candidate have a shower roundness less than 0.4. In addition, I required that the central crystal of this shower not be in one of the edge rings of the BGO.[16]

As shown in Figure 7.8, photons produced in the neutralino decays were expected to be energetic. Therefore, an event was not selected if any of the photon candidates had an energy below 20 GeV. This cut significantly reduced the background from cosmic rays. To further reduce cosmic contamination, I required that there should be at least one scintillator hit in time with the beam crossing within ±5 ns.

No candidate events were observed in the data after applying these cuts. Figure 7.13a shows that the cut on the shower roundness eliminated almost all background from the Standard Model processes. The residual background from the reaction $e^+e^- \to \nu\bar{\nu}\gamma(\gamma)$ was found to be 0.3 ± 0.1 events. The cosmic contamination was estimated using the methods described in Section 6.3.5 and found to be 0.2 ± 0.1 events.

---

[15] That is, I relaxed the cuts on the shower roundness and S_9^c/S_{25}^c variable (see Section 6.3.1).

[16] Shower leakage into the gaps between the BGO barrel and endcaps affected the measurement of the shower roundness. This effect can be seen by comparing Figures 6.3e and 6.3f (p. 142). The shower leakage effects were also discussed in Section C.2 of Appendix C.

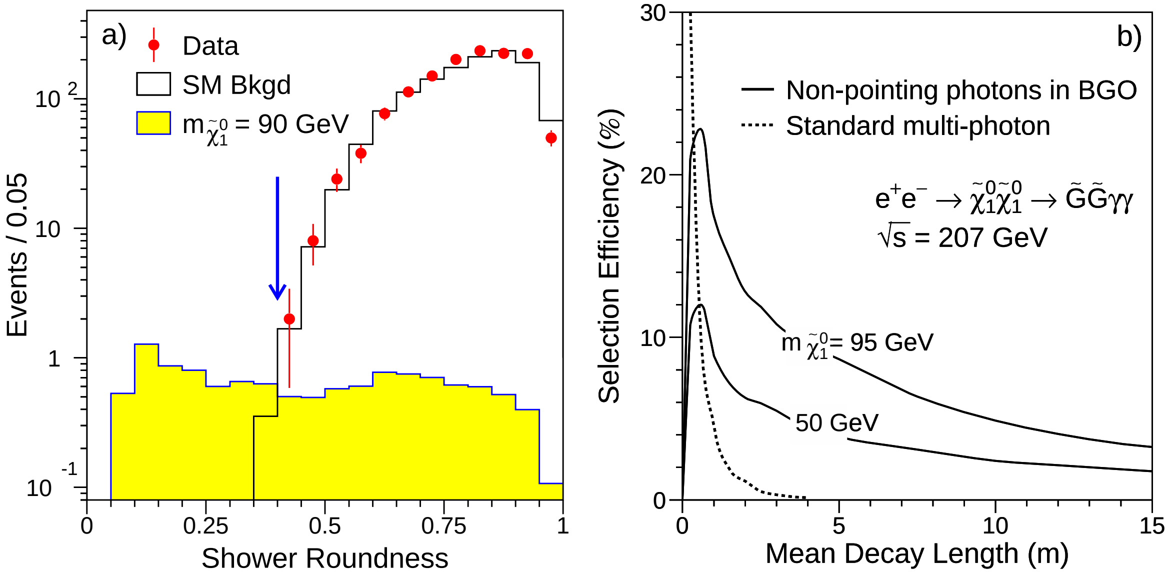

Figure 7.13: a) Distribution of the shower roundness for a sample of fully simulated $e^+e^- \to \tilde{\chi}_1^0\tilde{\chi}_1^0 \to \tilde{G}\tilde{G}\gamma\gamma$ events after all other selection cuts have been applied. The signal events were generated for a mean decay length of $L_{\tilde{\chi}_1^0} =$ 3 m and $m_{\tilde{\chi}_1^0} =$ 90 GeV. The arrow indicates the value of the cut. Also shown are the corresponding distributions for the data and the Standard Model background. The normalization for the signal is arbitrary. b) Selection efficiency as a function of the neutralino mean decay length for the standard multi-photon and the BGO-based non-pointing photon selections.

The efficiency of this selection was estimated using large samples of Monte Carlo events generated for $\tilde{\chi}_1^0$ decay lengths up to 100 m and processed through the full detector simulation. The signal efficiency was found to depend both on the neutralino mass and the neutralino lifetime. For lighter neutralinos, the majority of photons produced in the $\tilde{\chi}_1^0 \to \tilde{G}\gamma$ decays would be boosted in the direction of the neutralino's flight and, thus, eliminated by the cut on the shower roundness. Figure 7.13b shows the obtained signal efficiency as a function of the neutralino mean decay length in the laboratory frame ($L_{\tilde{\chi}_1^0}$). For $m_{\tilde{\chi}_1^0} = 95$ GeV and $\sqrt{s} = 207$ GeV, the efficiency reached a maximum value of about 25% at $L_{\tilde{\chi}_1^0} \simeq 1$ m and exponentially decreased after the peak. Figure 7.13b also shows that the "standard" multi-photon selection used in the previous section became ineffective for $L_{\tilde{\chi}_1^0} \geq 1$ m.

Non-pointing photons in the HCAL

In this analysis I made use of the barrel hadron calorimeter (HCAL) and the muon filter (see Figure 4.13 p. 82). An overview of these subdetectors was given in Section 4.2.5. The HCAL surrounded the BGO calorimeter and was made of depleted uranium and brass absorber plates interleaved with proportional wire chambers. The HCAL barrel was 4.7 m long and had an inner radius of about 0.9 m and an outer radius of about 1.8 m, covering the polar angle range $25° < \theta < 155°$. The signal wires of the proportional chambers were grouped to form readout towers which provided a segmentation of 10 layers in the radial direction. The amount of absorber material between two neighboring layers corresponded to about 10 radiation lengths (equivalent to approximately half a BGO crystal). Thus, the electromagnetic showers produced by photons and electrons in the HCAL were expected to be very compact.

The muon filter was designed to absorb the tail of hadronic showers and to track muons between the HCAL and the muon chambers. It was located just outside of the HCAL barrel and divided into eight octants, each made of six layers of brass absorber plates interleaved with five layers of proportional chambers. As described below, I used the muon filter to suppress the cosmic ray background. Since the HCAL endcaps were not covered by the muon filter, they were not used in this search.

Prior to their installation in L3, the assembled HCAL modules had been tested in beams of hadrons and electrons. These studies showed that the hadron calorimeter was capable of reconstructing not only hadronic but also electromagnetic showers [195].

In order to study the HCAL performance *in situ*, I used events from the Bhabha scattering process $e^+e^- \rightarrow e^+e^-$ in which both scattered electrons passed through the gaps between the BGO barrel and endcaps and produced two showers in the HCAL barrel. An example of such an event is displayed in Figure 7.14. In 1996 the gaps between the BGO barrel and endcaps were equipped with the EGAP calorimeter. Therefore, for this study I used 30 pb^{-1} of data collected by L3 in 1995 at or near the Z resonance, $\sqrt{s} \simeq 91$ GeV.

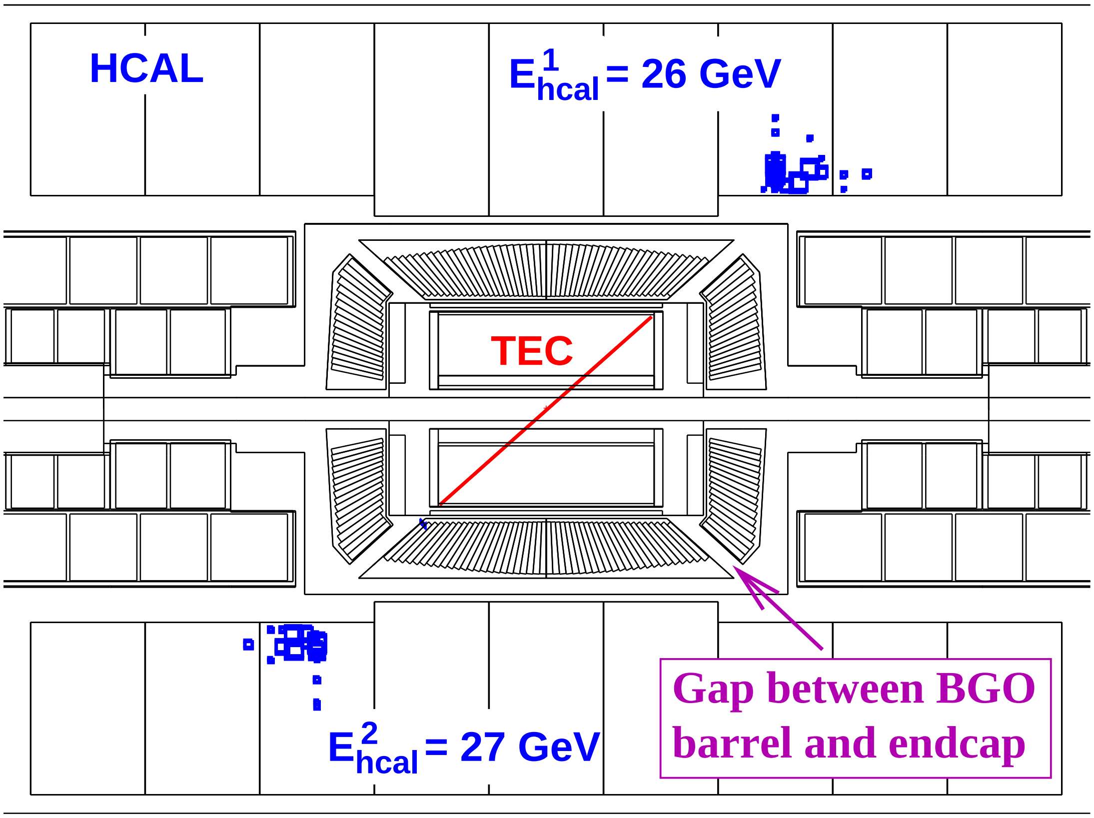

Figure 7.14: Display of a typical $e^+e^- \to e^+e^-$ event in which both electrons produced showers in the hadron calorimeter. This candidate event was recorded in 1995 at $\sqrt{s}$ = 91 GeV. The L3 detector is displayed in a plane parallel to the beam axis. Tracks reconstructed in the TEC are shown as back-to-back lines, and hits in the HCAL are shown as squares whose size is proportional to the deposited energy.

To select Bhabha events with electrons in the HCAL, I required two back-to-back clusters in the hadron calorimeter and no significant energy deposits in the BGO and forward calorimeters. In particular, I rejected events with a total energy deposited in the BGO above 1 GeV. In total, I selected 1,110 such events in data with about 1,048 expected from Monte Carlo.

Figure 7.15a shows the measured energy spectrum of the selected Bhabha electrons. The relative energy resolution of the HCAL for 45 GeV electrons was found to be $\sigma_{DATA} = 23\%$, in good agreement with the resolution predicted by the detector simulation $\sigma_{MC} = 21\%$. Since the HCAL calorimeter was calibrated using hadronic

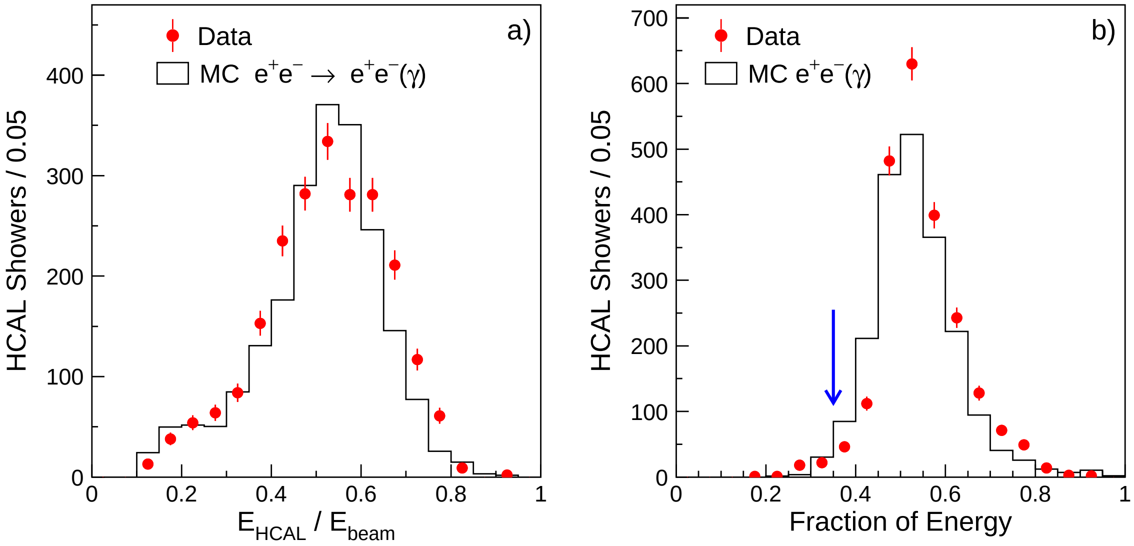

Figure 7.15: Distributions a) of the reconstructed shower energy and b) of the fraction of the shower energy deposited in the central layer for Bhabha events with showers in the HCAL. The event sample was selected using the L3 data collected in 1995 at $\sqrt{s} = 91$ GeV.

jets, for such highly energetic electromagnetic showers its energy scale was below one. The relative energy scale was measured to be $P_{DATA} = 0.54$, in good agreement with the prediction of the detector simulation $P_{MC} = 0.53$. These measurements are consistent with the results of a similar study described in Reference [196].

The test beam studies showed that electromagnetic showers could be distinguished from hadronic ones using a quantity T_1, defined as a ratio of energy deposited in the layer with the maximum energy deposition to the total shower energy. Since showers produced by electrons and photons were expected to be very compact, a cut $T_1 > 0.35$ eliminated only about 2% of such showers (see Figure 7.15b). In contrast, most of the hadronic showers did not survive this cut [195].

The above study demonstrated that the hadron calorimeter could be used to search for $e^+e^- \to \tilde{\chi}^0_1\tilde{\chi}^0_1$ events in which one or both of the neutralinos decayed in the HCAL. To select candidate events, I required one or two isolated clusters in the HCAL, each with a reconstructed shower energy above 15 GeV and $T_1 > 0.35$. There should be no other activity in the detector apart from what was consistent with noise. In particular, an event was rejected if more than 1 GeV was deposited in the BGO or EGAP calorimeters within a 15° cone around the cluster in the HCAL. I found that this requirement eliminated all background from Standard Model processes. By studying a sample of events randomly triggered at the beam crossing time (see Section 6.3.7), I also found that such highly energetic clusters could not be produced by the electronic and uranium noise in the HCAL.

However, an important source of background came from cosmic ray events. Cosmic muons traversing the hadron calorimeter could emit a a bremsstrahlung photon[17] and, thus, fake a non-pointing photon produced in the neutralino decay. Figure 7.16 shows a typical cosmic ray event with a bremsstrahlung photon in the HCAL.

To suppress this source of background, I required that there should be no track segments detected in any layer of the muon chambers $N_{\mathrm{MUTK}}=0$ and no hits in the muon filter $N_{\mathrm{M}F}=0$. No candidate events were found in the data after applying these anti-cosmic cuts. To estimate the expected cosmic ray background, I used a sample of $N_0 = 179$ events which satisfied all other selection criteria. Of these, 172 events were eliminated by the cut $N_{\mathrm{MUTK}}=0$ and 166 events by the cut $N_{\mathrm{M}F}=0$, which corresponded to rejection powers of $R_{\mathrm{MUTK}}=96 \pm 2\%$ and $R_{\mathrm{M}F}=92 \pm 2\%$, respectively.[18] Then, the expected cosmic contamination could be calculated as $N_{\mathrm{cosm}} = N_0 \cdot (1 - R_{\mathrm{MUTK}}) \cdot (1 - R_{\mathrm{M}F}) = 0.6 \pm 0.4$ events.

Events with non-pointing photons in the HCAL could be triggered only by the HCAL energy trigger. To estimate the efficiency of this trigger, I used cosmic ray events since such events could also be accepted by the muon trigger. In total, I selected 257 such cosmic ray events with a single HCAL cluster above 15 GeV, of which 242 events were also accepted by the HCAL energy trigger. Thus, the HCAL trigger efficiency was estimated to be $\varepsilon_{Data} = 94 \pm 1\%$, in good agreement with the Monte Carlo prediction of $\varepsilon_{MC} = 96\%$.

The efficiency of this selection was estimated using large samples of fully simulated $\mathrm{e}^+\mathrm{e}^- \to \tilde{\chi}_1^0\tilde{\chi}_1^0$ events generated for $\tilde{\chi}_1^0$ decay lengths up to 100 m. As shown in

---

[17] This production mechanism was described in detail in Section 6.3.5.

[18] The rejection power of the cut $N_{\mathrm{MUTK}}=0$ was cross checked using a sample of out-of-time cosmic events as described in Section 6.3.5. The rejection power of the cut $N_{\mathrm{M}F}=0$ was in agreement with an estimate of 91% provided by earlier tests of the performance of the muon filter [128].

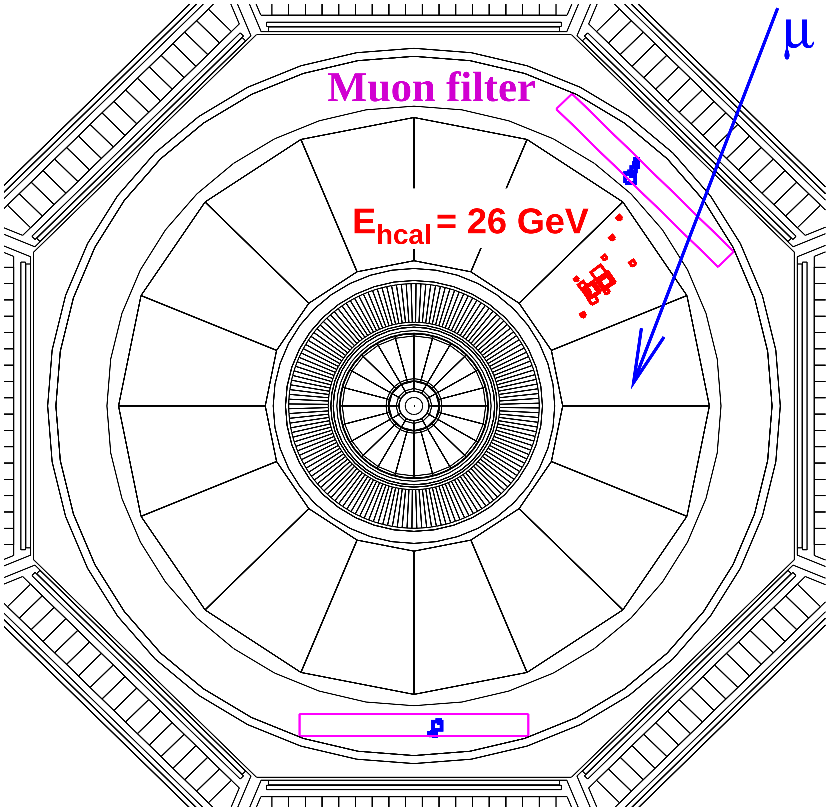

Figure 7.16: A cosmic ray event in which the cosmic muon emitted a bremsstrahlung photon in the HCAL. The event is displayed in the plane perpendicular to the beam axis. The arrow indicates the flight direction of the cosmic muon, as determined from the two clusters in the muon filter.

Figure 7.17a, the signal efficiency reached a maximum of 15% at $L_{\tilde{\chi}_1^0} \simeq 3$ m and, for larger lifetimes, was significantly higher than the efficiency of the BGO-based selection. In addition, the HCAL-based selection was not sensitive to the flight direction of the photon candidates and, therefore, its efficiency was almost the same for all allowed values of the neutralino mass. In contrast, the BGO-based search became ineffective for $m_{\tilde{\chi}_1^0} \lesssim 50$ GeV.

Non-pointing photons in the BGO and HCAL

This unique event topology could be produced if one of the neutralinos decayed in front of the BGO calorimeter and the other in the HCAL as shown in Figure 7.12. For this search I required a shower in the BGO with an energy above 20 GeV and a cluster in the HCAL with an energy above 15 GeV. There should be no other activity in the detector apart from what was consistent with noise. To reject single-photon events with shower leakage from the BGO into the HCAL, I required that the two photon candidates be separated by more than 20°.

No data events satisfied these selection criteria and no events were expected from Standard Model processes. The efficiency of this selection for the process $e^+e^-\to\tilde{\chi}^0_1\tilde{\chi}^0_1$ is shown in Figure 7.17a as a function of the neutralino decay length. It reached a maximum value of about 20% at $L_{\tilde{\chi}^0_1}\simeq 1$ m and rapidly decreased after the peak. This search strategy became ineffective for $L_{\tilde{\chi}^0_1}\gtrsim 10$ m since such lifetimes would have implied that at least one of the produced neutralinos decayed outside the detector.

Results

Since signal events could not be accepted by more than one selection, the total signal efficiency was obtained by adding together the efficiencies of the three individual selections. The total signal efficiency is shown in Figure 7.17b as a function of the $\tilde{\chi}^0_1$ decay length for three mass hypotheses: $m_{\tilde{\chi}^0_1} = 95, 50,$ and 10 GeV. The signal efficiency increases with the neutralino mass, reaching a maximum value of about 40% at $L_{\tilde{\chi}^0_1}\simeq 1.5$ m near the kinematic limit $m_{\tilde{\chi}^0_1}=\sqrt{s}/2$.

No candidate events had been found for any of the final state topologies, and upper limits on the signal cross section were derived using the statistical procedure described in Section 7.2.1. For $L_{\tilde{\chi}^0_1}\leq 2\,\mathrm{m}$, the limits were derived by combining the results of the searches for the non-pointing photon and standard multi-photon[19] signatures. The obtained limits on the $e^+e^-\to\tilde{\chi}^0_1\tilde{\chi}^0_1$ cross section at $\sqrt{s}=207$ GeV are shown in Figure 7.10c as a function of the $\tilde{\chi}^0_1$ decay length. Data collected at lower $\sqrt{s}$ were included assuming the signal cross section to scale according to the MGM model [194], which was discussed in the previous section.

The systematic error on efficiency of the non-pointing selection was dominated by the systematic errors associated with the modelling of the shower development and the uncertainty on the HCAL trigger efficiency. It was estimated to be at most 5%

---

[19] The search for multi-photon $e^+e^-\to\tilde{\chi}^0_1\tilde{\chi}^0_1\to\tilde{G}\tilde{G}\gamma\gamma$ events was described in the previous section.

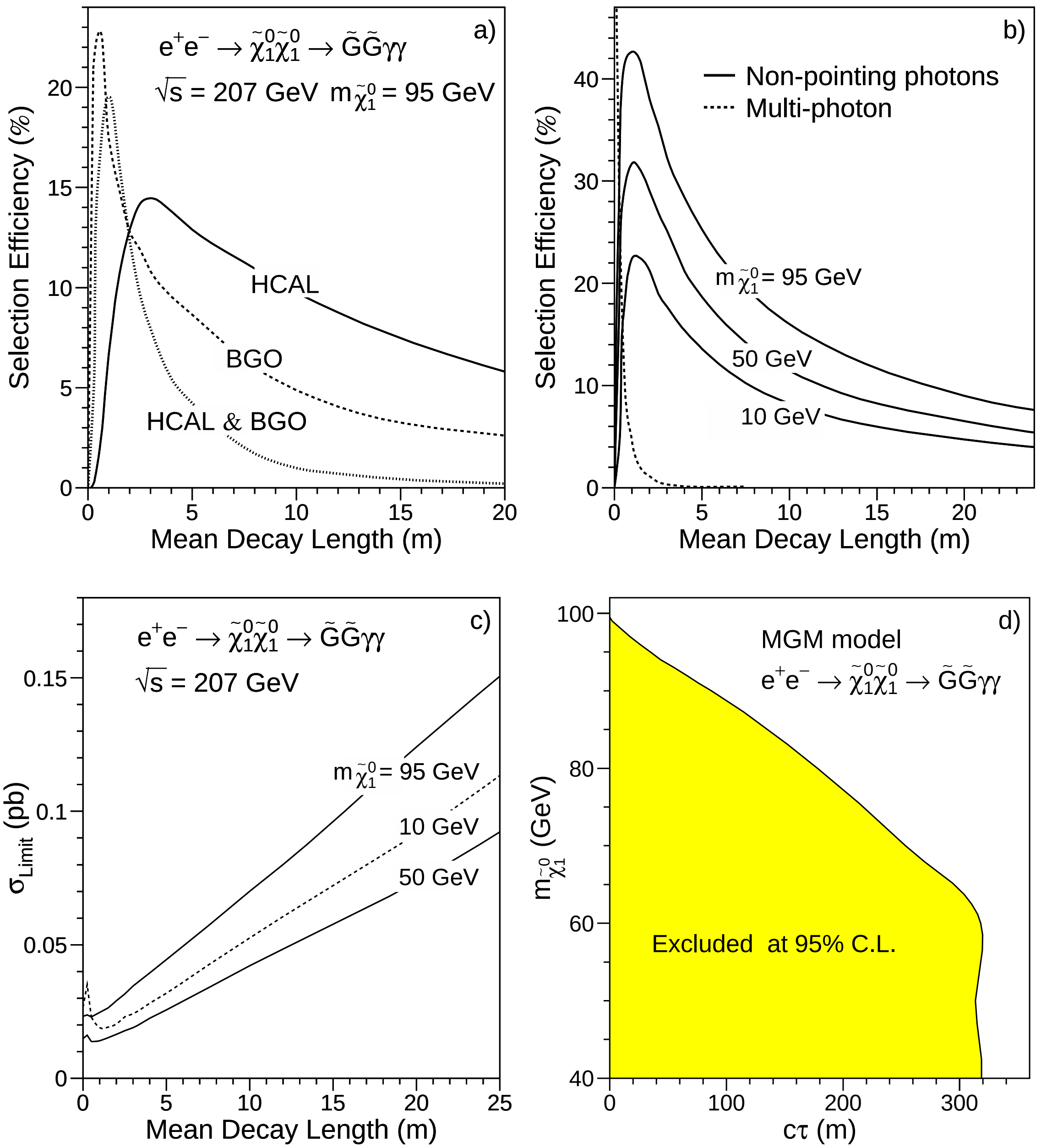

Figure 7.17: **a)** Efficiencies for the HCAL-based, BGO-based, and HCAL+BGO selections of $e^+e^-\rightarrow\tilde{\chi}_1^0\tilde{\chi}_1^0\rightarrow\tilde{G}\tilde{G}\gamma\gamma$ events with non-pointing photons for $m_{\tilde{\chi}_1^0} = 95$ GeV and $\sqrt{s} = 207$ GeV. **b)** Signal efficiencies and **c)** upper limits at the 95% C.L. on the production cross section for three different neutralino mass hypotheses $m_{\tilde{\chi}_1^0} = 95, 50, \text{and}\, 10$ GeV. Data collected at lower $\sqrt{s}$ were included assuming the signal cross section to scale according to the MGM model [194]. All curves are shown as a function of the neutralino mean decay length in the laboratory frame. **d)** Region excluded in the $(c\tau_{\tilde{\chi}_1^0}, m_{\tilde{\chi}_1^0})$ plane at the 95% C.L. under the assumptions of the MGM.

N_{mess}	1	2	3	4
Λ (TeV)	61.5	36.3	25.5	20.3
M_{mess} (TeV)	75	130	10^5	$5.6 \cdot 10^6$
$m_{\tilde{\mathrm{G}}}$ (eV)	1.1	1.2	620	$2.7 \cdot 10^4$
$m_{\tilde{\chi}^0_1}$ (GeV)	78.6	83.8	88.0	104.2
$m_{\tilde{\tau}_1}$ (GeV)	82.1	87.1	90.8	106.3
$m_{\tilde{\mathrm{e}}_\mathrm{R}}, m_{\tilde{\mu}_\mathrm{R}}$ (GeV)	107.6	102.2	92.1	107.1

Table 7.3: Lower limits at the 95% C.L. on the universal mass scale of the SUSY particles Λ, the messenger mass scale M_{mess}, and the gravitino, neutralino, and slepton masses as functions of the number of messenger pairs N_{mess}. The limits were derived from a scan over the parameter space of the minimal GMSB model, assuming the $\tilde{\chi}^0_1$ NLSP scenario with $L_{\tilde{\chi}^0_1} \leq 100\,\mathrm{m}$.

and had a negligible effect on the derived limits.

In the framework of the MGM model, the cross section limits can be translated into an excluded region in the $(c\tau_{\tilde{\chi}^0_1}, m_{\tilde{\chi}^0_1})$ plane. Here, $\tau_{\tilde{\chi}^0_1}$ denotes the proper lifetime of the neutralino, which is related to mean decay length in the laboratory frame through $L_{\tilde{\chi}^0_1} = \gamma\beta c\tau_{\tilde{\chi}^0_1}$. As shown in Figure 7.17d, neutralino masses below 88.6 GeV were excluded for $c\tau_{\tilde{\chi}^0_1}$ values smaller than 100 m.

The results of this search can also be interpreted in the framework of the minimal gauge-mediated SUSY breaking (GMSB) model. The assumptions and parameters of this model were described in Section 3.1.3 (p. 38).

To set limits on the model parameters and masses of SUSY particles, a scan over the GMSB parameter space was performed [197]. In total, $5.6 \cdot 10^6$ points in the parameter space were tested. At each point the complete mass spectrum, production cross sections, and branching ratios were calculated using the `ISAJET` program [198]. A point in the parameter space was excluded if it was kinematically accessible and the expected $\mathrm{e}^+\mathrm{e}^- \to \tilde{\chi}^0_1\tilde{\chi}^0_1$ cross section was higher than my cross section limit for the corresponding $\tilde{\chi}^0_1$ mass. In addition, the Higgs boson masses and couplings were also computed and the lower limit on the Higgs mass, $m_\mathrm{h} > 84.5$ GeV [199], was used to extend the exclusion domain. The results of this scan are summarized in Table 7.3.

7.3 Searches for Extra Dimensions

Models with large extra dimensions predict a gravity scale (M_D) as low as the electroweak scale. In such models, gravitons may be produced via the $\mathrm{e^+e^-} \to \gamma\mathrm{G}$ process as described in Section 3.3.1 of Chapter 3. Since the graviton would escape undetected, this reaction could provide a new source of single-photon events at LEP.

To calculate the predicted signal rates and distributions, I used the results of the single- and soft-photon selections (Sections 6.3.8 and 6.5). The efficiency for the $\mathrm{e^+e^-} \to \nu\bar{\nu}\gamma$ process was derived in an x_γ *vs.* $|\cos\theta_\gamma|$ grid similar to that of Table D.3 (p. 296). This grid, together with the analytical differential cross section (see Equation 3.29 p. 57), allowed me to calculate the signal efficiencies and expectations as a function of M_D and the number of extra dimensions (n). Effects of initial-state radiation were taken into account using the radiator function given in Reference [20].

To check the validity of this method, I applied the same procedure to the gravitino pair-production process, $\mathrm{e^+e^-} \to \tilde{\mathrm{G}}\tilde{\mathrm{G}}\gamma$. The kinematic distributions of photons from this process were similar to those of the extra dimensions signals. However, in this case the signal expectations could also be obtained from a large sample of fully simulated Monte Carlo events (see Section 7.2.2). The signal efficiencies calculated using the grid method and the Monte Carlo sample were found to be consistent within their statistical errors.

Since the energy spectrum of the photons produced in the $\mathrm{e^+e^-} \to \gamma\mathrm{G}$ process was expected to be soft, only events from the single- and soft-photon samples with $x_\gamma < 0.5$ were considered. In total, I selected 1,286 such events in data with 1,303.6 events expected from Standard Model processes. Expected effects of extra dimensions on the energy and polar angle distributions are shown in Figure 7.18. The signal efficiency was found to slightly decrease with n: from 63% for $n = 2$ to 59% for $\mathrm{n} = 8$.

No excess was observed beyond the Standard Model expectation, and limits on the graviton-photon emission were derived from a likelihood fit to the x_γ *vs.* $|\cos\theta_\gamma|$ two-dimensional distribution. Since the signal cross section scaled with $(1/M_D)^{n+2}$, this variable was taken as the fit parameter. The results of the fit are given in Table 7.4,

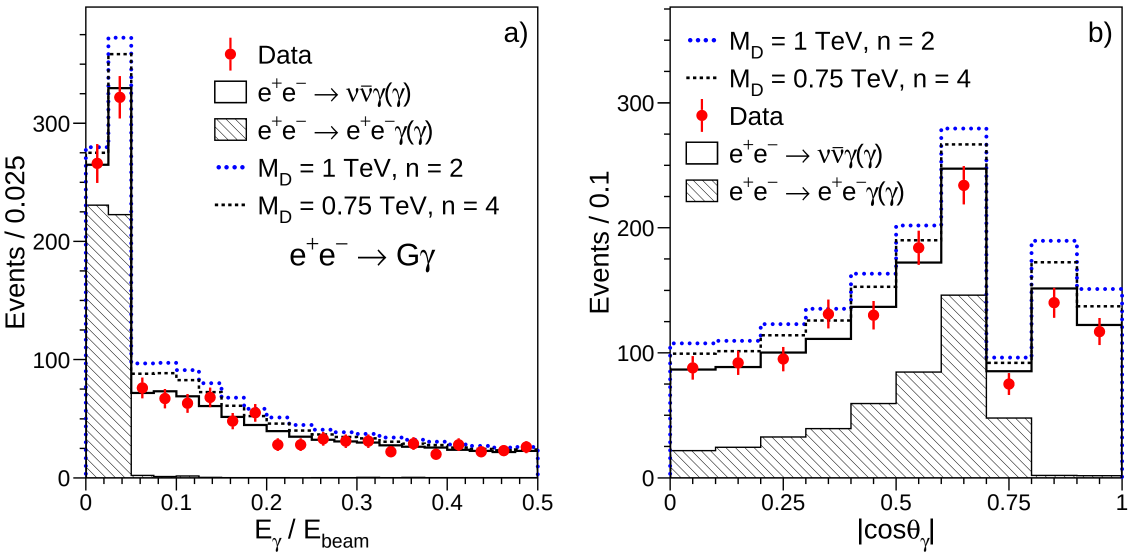

Figure 7.18: Distributions of a) the ratio of the photon energy to the beam energy (x_γ) and b) the photon polar angle for events with $x_\gamma < 0.5$ from the combined single- and soft-photon sample. Signals for extra dimensions for $M_D = 1$ TeV and 0.75 TeV and $n = 2$ and 4 are also shown.

where the error on the parameter $(1/M_D)^{n+2}$ corresponds to a change in the negative log-likelihood with respect to its minimum of 0.5. Table 7.4 also lists the observed and expected limits on the new scale of gravity and on the size of extra dimensions. These limits were derived following the statistical procedure described in Section 7.2.1.

The combination of my results with those of other LEP experiments will be described in Appendix E. The LEP combined search excluded, at the 95% C.L., the gravity scales below 1.6 TeV and 0.66 TeV for $n = 2$ and $n = 6$, respectively.

Searches for Branons

In models with extra dimensions the presence of a three-dimensional brane as an additional physical body leads to the appearance of additional degrees of freedom. These may manifest themselves as new scalar particles, $\tilde{\pi}$, called branons. As described in Section 3.3.2, branons could be pair-produced at LEP in the reaction $e^+e^- \to \tilde{\pi}\tilde{\pi}\gamma$. Because branons do not interact in the detector, this process would to lead to a single photon and missing energy in the final state. The signal cross section depends only

n	$(1/M_D)^{n+2}$	M_{D95} (TeV)	M_{exp} (TeV)	R_{95} (cm)	CL$_b$
2	-0.03 ± 0.10 TeV $^{-4}$	1.50	1.49	2.1×10^{-2}	43%
3	-0.10 ± 0.28 TeV $^{-5}$	1.14	1.12	2.9×10^{-7}	40%
4	-0.5 ± 1.0 TeV $^{-6}$	0.91	0.89	1.1×10^{-9}	37%
5	-2.2 ± 3.9 TeV $^{-7}$	0.76	0.75	4.2×10^{-11}	38%
6	-11.2 ± 17.7 TeV $^{-8}$	0.65	0.64	4.7×10^{-12}	37%
7	-67 ± 87 TeV $^{-9}$	0.57	0.56	1.0×10^{-12}	34%
8	-400 ± 460 TeV $^{-10}$	0.51	0.51	3.2×10^{-13}	35%

Table 7.4: Fitted values of $(1/M_D)^{n+2}$ together with the observed (M_{D95}) and expected (M_{exp}) lower limits on the gravity scale as a function of the number of extra dimensions (n). Upper limits on the size of the extra dimensions (R_{95}) are also given. All limits are at the 95% confidence level. Assuming there is no signal, CL$_b$ gives the probability to obtain a limit on M_D better than the one observed.

on two parameters: the brane tension f and the branon mass M_π.

The signal properties were expected to be very similar to those of the graviton-photon emission considered above so that the same analysis procedure could be used. Figure 7.19a shows how the branon production was expected to affect the photon energy spectrum. Since no deviations from the Standard Model predictions were observed, limits on the branon production were derived from a fit to the x_γ *vs.* $|\cos\theta_\gamma|$ two-dimensional distribution. The region excluded in the (f, M_π) plane is shown in Figure 7.19b. In the massless branon scenario, the brane tension must be greater than 180 GeV, whereas for very elastic branes ($f \rightarrow 0$) branon masses below 103 GeV were excluded at the 95% confidence level [200].

7.4 Measurements of Gauge-Boson Couplings

In the previous sections I described how I searched for manifestations of new physics by searching for evidence of new processes leading to photonic events with missing energy. The existence of anomalous couplings between the photon and heavy gauge bosons is expected to affect the $e^+e^- \rightarrow \nu\bar{\nu}\gamma(\gamma)$ process. Therefore, such deviations

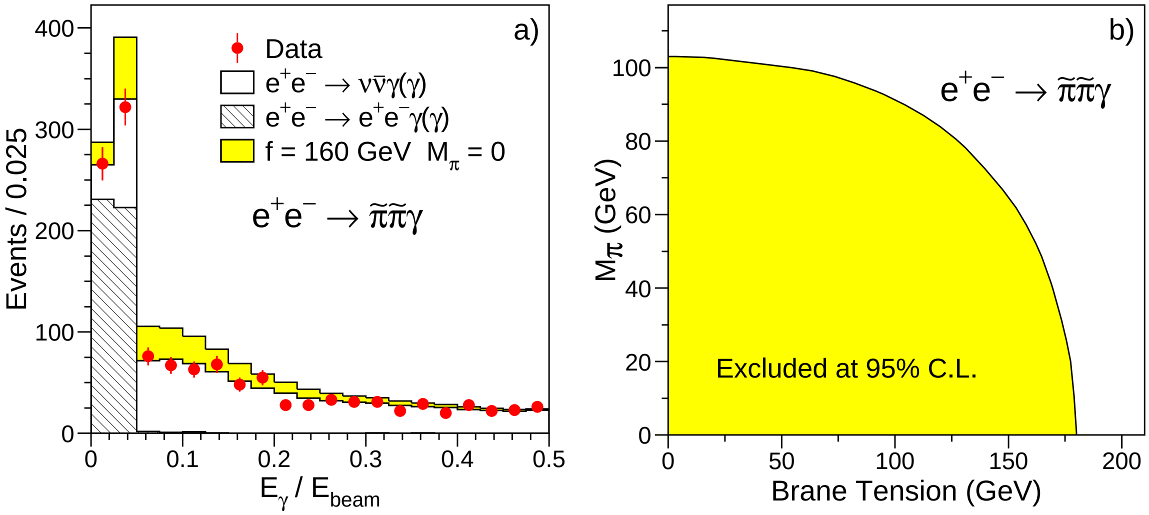

Figure 7.19: a) Distribution of the ratio of the photon energy to the beam energy (x_γ) for the combined single- and soft-photon event sample. Expected signal from the branon-photon production is also shown for $M_\pi = 0$ and $f = 160$ GeV. b) Region in the (f, M_π) plane excluded by this search.

from the Standard Model can be probed directly by measuring the total and differential cross sections of this process. Below I describe how I used my single- and multi-photon samples to extract the triple and quartic gauge-boson couplings, respectively. The corresponding event selections were described in Sections 6.3.8 and 6.4, where I also showed that the purities of the selected $\nu\bar{\nu}\gamma$ and $\nu\bar{\nu}\gamma\gamma$ event samples were estimated to be higher than 99%.

7.4.1 Searches for Anomalous Quartic Gauge Couplings

In the Standard Model self-interactions of the vector boson fields arise due to the $-\frac{1}{4}\mathbf{W}_{\mu\nu} \cdot \mathbf{W}^{\mu\nu}$ term in the electroweak Lagrangian (see Equation 2.10 p. 11). In addition to the triple gauge couplings, this term leads to quartic gauge couplings (QGCs) of the form: WWWW, WWZZ, WW$\gamma\gamma$, and WWZγ. The strength of the coupling at these vertices is specified by the $SU(2) \times U(1)$ gauge invariant form of the electroweak sector. Studying processes to which these QGCs can contribute may therefore yield further confirmation of the non-Abelian structure of the Standard Model or signal the presence of new physics at as yet unprobed energy scales. Unfortunately, the

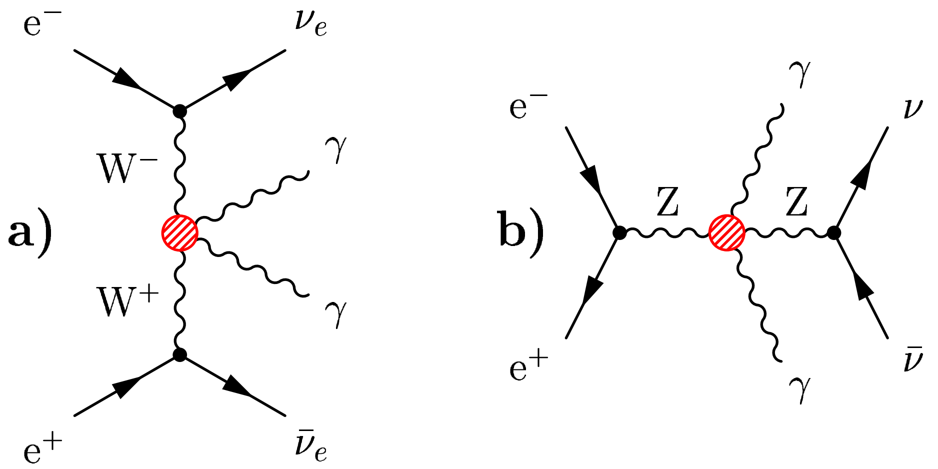

Figure 7.20: Feynman diagrams contributing to the $e^+e^- \rightarrow \nu\bar{\nu}\gamma\gamma$ process and containing the a) $W^+W^-\gamma\gamma$ and b) $ZZ\gamma\gamma$ vertices.

contributions of the Standard Model QGCs are too small to be directly observed at LEP2 energies. For instance, the contribution of the $W^+W^-\gamma\gamma$ vertex (Figure 7.20a) to the cross section of the $e^+e^- \rightarrow \nu\bar{\nu}\gamma\gamma$ process is only about 1-2 fb [201].

The triple and quartic gauge-boson couplings probe different aspects of the weak interactions. The triple gauge couplings directly test the non-Abelian gauge structure. Their possible deviations from the Standard Model predictions have been extensively studied and tightly constrained by measurements of the $e^+e^- \rightarrow W^+W^-$ production at LEP2 [202].

In contrast, the quartic couplings can be regarded as a more direct window on electroweak symmetry breaking or, more generally, on new physics which couples to electroweak bosons. In this respect it is quite possible that the quartic couplings deviate from their Standard Model values while the triple gauge couplings do not [203]. For example, if the mechanism of electroweak symmetry breaking does not reveal itself through the discovery of new particles such as the Higgs boson, supersymmetric particles, or technipions, it is possible that anomalous quartic couplings can provide the first evidence of new physics in this sector of the electroweak theory [204].

Parametrization of Quartic Gauge Couplings

The formalism for the extra genuine quartic terms has been developed in Reference [205]. Here, genuine quartic terms refer to those that give no contribution to the triple-gauge-boson vertices. In this parametrization, the two lowest dimension terms that give rise to genuine quartic couplings involving at least one photon are

$$\begin{aligned} \mathcal{L}_6^0 &= -\frac{e^2}{16}\frac{a_0}{\Lambda^2}F_{\mu\nu}F^{\mu\nu}\vec{W}^{\alpha}\cdot\vec{W}_{\alpha}, \\ \mathcal{L}_6^{\mathrm{c}} &= -\frac{e^2}{16}\frac{a_{\mathrm{c}}}{\Lambda^2}F_{\mu\alpha}F^{\mu\beta}\vec{W}^{\alpha}\cdot\vec{W}_{\beta}, \end{aligned} \tag{7.20}$$

where $F^{\mu\nu} = \partial_\mu A_\nu - \partial_\nu A_\mu$ is the photon field strength tensor. These are obtained by assuming C and P conservation and imposing the $U(1)$ gauge invariance and the global custodial $SU(2)$ symmetry that keeps the $\rho = M_W/M_Z\cos^2\theta_W$ parameter close to the measured value of 1.

The custodial $SU(2)$ field vector is given by

$$\vec{W}_\alpha = \begin{pmatrix} \frac{1}{\sqrt{2}}(W_\alpha^+ + W_\alpha^-) \\ \frac{i}{\sqrt{2}}(W_\alpha^+ - W_\alpha^-) \\ Z_\alpha/\cos\theta_W \end{pmatrix},$$

which yields in terms of the physical fields W_α^+, W_α^- and Z_α:

$$\begin{aligned} \mathcal{L}_6^0 &= -\frac{e^2}{8}\frac{a_0^{\mathrm{W}}}{\Lambda^2}F_{\mu\nu}F^{\mu\nu}W^{+\alpha}W_\alpha^- - \frac{e^2}{16\cos^2\theta_W}\frac{a_0^{\mathrm{Z}}}{\Lambda^2}F_{\mu\nu}F^{\mu\nu}Z^\alpha Z_\alpha, \\ \mathcal{L}_6^{\mathrm{c}} &= -\frac{e^2}{16}\frac{a_{\mathrm{c}}^{\mathrm{W}}}{\Lambda^2}F_{\mu\alpha}F^{\mu\beta}(W^{+\alpha}W_\beta^- + W^{-\alpha}W_\beta^+) - \frac{e^2}{16\cos^2\theta_W}\frac{a_{\mathrm{c}}^{\mathrm{Z}}}{\Lambda^2}F_{\mu\alpha}F^{\mu\beta}Z^\alpha Z_\beta\,. \end{aligned}$$

Therefore, both the $\mathcal{L}_6^0$ and $\mathcal{L}_6^{\mathrm{c}}$ Lagrangian terms give rise to the $\mathrm{W}^+\mathrm{W}^-\gamma\gamma$ and $\mathrm{ZZ}\gamma\gamma$ interactions, which can be described by two sets of anomalous QGCs: $\{a_0^{\mathrm{W}}, a_{\mathrm{c}}^{\mathrm{W}}\}$ and $\{a_0^{\mathrm{Z}}, a_{\mathrm{c}}^{\mathrm{Z}}\}$. The $\mathrm{W}^+\mathrm{W}^-\gamma\gamma$ and $\mathrm{ZZ}\gamma\gamma$ couplings can be assumed to be independent, as suggested by a more general treatment of quartic terms performed in Reference [206]. In all cases the strengths of the quartic couplings are proportional to $1/\Lambda^2$, where Λ is interpreted as the energy scale of the new physics.

Sensitivity of the $e^+e^- \to \nu\bar{\nu}\gamma\gamma$ Process to Anomalous QGCs

The $W^+W^-\gamma\gamma$ and $ZZ\gamma\gamma$ interactions are expected to affect the $e^+e^- \to \nu\bar{\nu}\gamma\gamma$ process in a different manner [201, 207]. The existence of $W^+W^-\gamma\gamma$ anomalous QGCs leads to the WW−fusion $e^+e^- \to \nu_e\bar{\nu}_e\gamma\gamma$ process as shown in Figure 7.20a. The majority of signal events are expected to be produced in the recoil mass region below the Z-return peak, $M_{\rm rec} \lesssim 80$ GeV, where the Standard Model background is very low.[20]

On the other hand, the existence of the $ZZ\gamma\gamma$ vertex affects the $e^+e^- \to \nu\bar{\nu}\gamma\gamma$ process via the s-channel Z exchange diagram (see Figure 7.20b). This contribution is expected to increase the production cross section in the region of the Z-return peak, $80 < M_{\rm rec} < 120$ GeV, since the Z bosons are produced mostly on-shell. Thus, the $W^+W^-\gamma\gamma$ and $ZZ\gamma\gamma$ interactions are expected to manifest themselves in different regions of the recoil mass spectrum. However, in both cases the anomalous contributions would lead to an excess of multi-photon events with two energetic photons.[21]

Figure 7.21a shows that the production cross section depends quadratically on the anomalous QGCs. Figures 7.21a,b also show that the size of anomalous contributions increases rapidly with the center-of-mass energy.

In order to search for manifestations of anomalous QGCs, I used the sample of multi-photon events selected at $\sqrt{s} = 189 - 208$ GeV as described in Section 6.4. The Standard Model contributions were further suppressed by requiring that the recoil mass to the multi-photon system should be below 140 GeV, $M_{\rm rec} < 140$ GeV, and the energy of the second most energetic photon should be above 5 GeV, $E_{\gamma_2} > 5$ GeV.

After these cuts, 38 events were selected in the data while 45.4 events were expected from the Standard Model $e^+e^- \to \nu\bar{\nu}\gamma\gamma$ process. In this analysis the Standard Model predictions and anomalous contributions were simulated using the latest version of the `NUNUGPV` Monte Carlo program [207]. The independent `KKMC` program was used as a cross check on the Standard Model expectations.

---

[20] In the Standard Model the reaction $e^+e^- \to \nu\bar{\nu}\gamma\gamma$ proceeds mainly via initial state radiation from the incoming electrons and positrons. As discussed in Section 2.2.2, the recoil mass distribution has a peak near $M_{\rm rec} \simeq M_Z$, while the energy spectrum for the second most energetic photon is expected to be soft.

[21] The form of the quartic terms $\mathcal{L}_6^0$ and $\mathcal{L}_6^c$ dictates that anomalous contributions to the $\nu\bar{\nu}\gamma\gamma$ matrix element scale linearly with the energy of the photons [201].

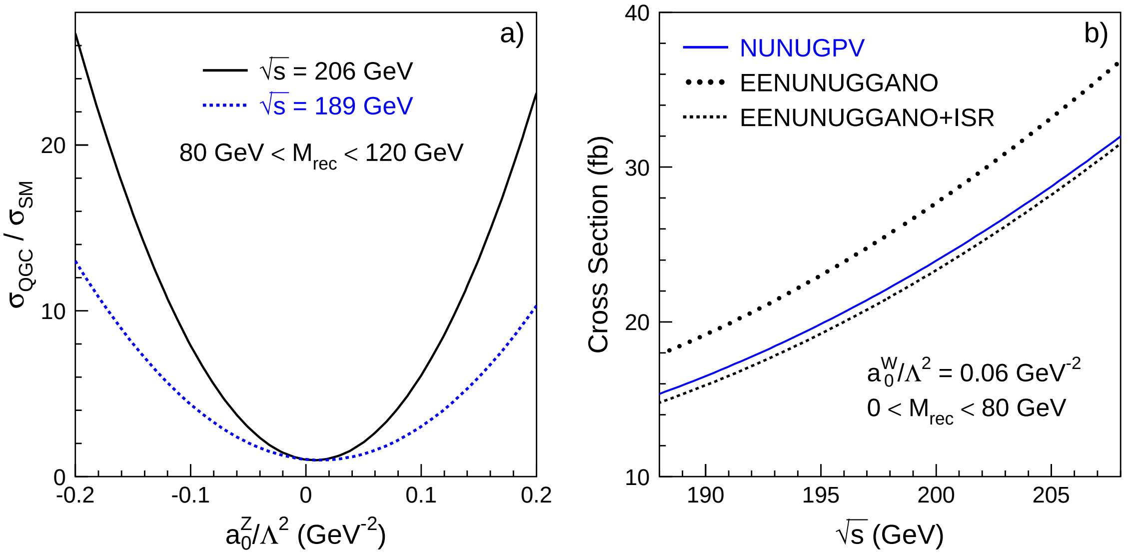

Figure 7.21: a) The ratio of the accepted $e^+e^- \rightarrow \nu\bar{\nu}\gamma\gamma$ cross section to the Standard Model prediction as a function of the coupling a_0^Z/Λ^2. The cross sections were calculated with the `NUNUGPV` program after applying the kinematic cuts $E_{\gamma_2} > 5$ GeV and $80 < M_{\rm rec} < 120$ GeV. b) The accepted cross section as a function of the $\sqrt{s}$ for $a_0^W/\Lambda^2 = 0.06\ \mathrm{GeV}^{-2}$, as predicted by the `NUNUGPV` and `Eenunuggano` programs. In this case the kinematic cuts were $E_{\gamma_2} > 5$ GeV and $M_{\rm rec} < 80$ GeV.

Figure 7.22 shows the obtained recoil mass and E_{γ_2} spectra for the selected multi-photon sample. The expected effects of anomalous QGCs on these distributions are also shown. In both cases the data were well described by the Standard Model expectations.

Fit Method and Systematic Errors

Constraints on anomalous QGCs were derived using the binned maximum likelihood method described by Equation 7.6 (p. 198). The fits were performed using two-dimensional $M_{\rm rec}$ *vs.* E_{γ_2} distribution. For a given set of quartic couplings $\Psi_{\rm fit}$ varied in the fit, the expectation was calculated by reweighting each Monte Carlo event with the ratio

$$R(p_n, \Psi_{\rm fit}, \Psi_{\rm gen}) = \frac{|\mathcal{M}(p_n, \Psi_{\rm fit})|^2}{|\mathcal{M}(p_n, \Psi_{\rm gen})|^2}\,, \qquad (7.21)$$

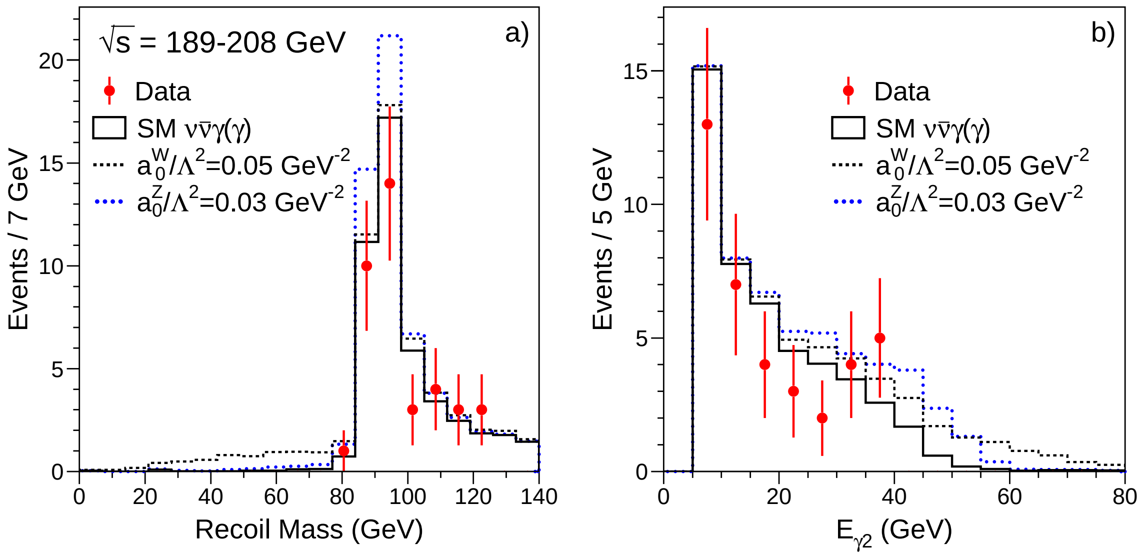

Figure 7.22: a) M_{rec} and b) E_{γ_2} spectra of the accepted multi-photon events. Also shown are the effects of possible anomalous QGCs for $a_0^{\mathrm{W}}/\Lambda^2 = 0.03\ \mathrm{GeV}^{-2}$ and $a_0^{\mathrm{W}}/\Lambda^2 = 0.05\ \mathrm{GeV}^{-2}$. In each case the other three anomalous QGCs were set to zero.

where $\mathcal{M}$ is the matrix element computed with the `NUNUGPV` program [207] using the generated four-momenta p_n and Ψ_{gen} denotes the QGC values with which this event was originally generated. The fitted values of couplings were then determined by maximizing the log-likelihood function.

One-parameter fits were performed by allowing one coupling to vary while fixing the others to the Standard Model values of zero. For such fits the 68% and 95% confidence intervals were obtained by finding the values of the fitted coupling that corresponded to a change in the negative log-likelihood with respect to its minimum of 0.5 and 1.92, respectively[22] (see also Equation 7.7 p. 199).

To estimate the systematic uncertainties on the measured couplings, I used the following method [185]. Let us assume that z is a parameter (e.g., selection efficiency) known with some limited accuracy: $z = z_0 \pm \sigma_z$. To estimate the impact of this systematic uncertainty σ_z on the measurement of a coupling α, the fit is repeated by

---

[22] For a non-Gaussian likelihood function these intervals do not correspond exactly to the claimed coverage probability [184]. However, this method was adopted by the L3 and LEP electroweak groups since it was relatively simple to use for the combination of several channels or experiments.

setting z in the Monte Carlo simulation to z_0, $z_0+\sigma_z$ and $z_0-\sigma_z$, giving

$$\begin{aligned} \alpha(z_0) &= \alpha_0 \pm \sigma_0\,, \\ \alpha(z_0+\sigma_z) &= \alpha_0 + \Delta\alpha_+ \pm \sigma_+\,, \\ \alpha(z_0-\sigma_z) &= \alpha_0 + \Delta\alpha_- \pm \sigma_-\,, \end{aligned}$$

where, for simplicity, the fit error is assumed to be symmetric and taken to be half the 68% C.L. interval. Then, the systematic error assigned to this source of uncertainty can be estimated as

$$(\delta\alpha)^2_z = \left(\frac{|\Delta\alpha_+| + |\Delta\alpha_-|}{2}\right)^2 + \max\left(\frac{\sigma^2_+ + \sigma^2_- - 2\sigma^2_0}{2}, 0\right)\,. \tag{7.22}$$

Thus, this method takes into account both the change in the sensitivity of the fit and the shift in the position of the maximum of the likelihood.

The main sources of systematic uncertainty are described below.

Contributions from anomalous QGCs: This error was estimated by calculating differences between the predictions of the `NUNUGPV` program and other theoretical calculations. For the $\mathrm{W^+W^-}\gamma\gamma$ couplings, the `NUNUGPV` was compared with the `Eenunuggano` program [201] as shown in Figure 7.21b. For the $\mathrm{Z Z}\gamma\gamma$ couplings, the predictions of Bélanger et al. [206] were used as a cross check. In both cases, the theoretical uncertainty on the signal cross section was estimated to be ±4%.

Standard Model $\nu\bar{\nu}\gamma\gamma$ cross section: The theoretical uncertainty on the accepted cross section of the Standard Model reaction $\mathrm{e^+e^-}\rightarrow\nu\bar{\nu}\gamma\gamma$ was assigned to be ±5% [24]. This estimate agreed well with the observed difference between the expectations of the `NUNUGPV` and `KKMC` Monte Carlo generators: 45.4 and 47.8 events, respectively.

Experimental uncertainties: The dominant experimental uncertainties came from the modelling of photon conversion effects and the systematic error on the trigger efficiency. The other considered systematic effects were the same as those studied in the context of the $\mathrm{e^+e^-}\rightarrow\nu\bar{\nu}\gamma(\gamma)$ cross section measurement (see Table 7.2). The total systematic error on the selection efficiency was estimated to be about 1.5%

For each center-of-mass energy, a sample of 10,000 $\nu\bar{\nu}\gamma\gamma$ events was generated and processed through the full L3 simulation. As a result, the related MC statistical error was negligible. In addition, the fitting and reweighting procedures were tested by fitting large Monte Carlo samples generated for different values of anomalous QGCs. No significant biases were observed.

Limits on Anomalous QGCs

Figures 7.23a-d show the log-likelihood curves derived from one-parameter fits to the four anomalous QGCs. The following 68% confidence level results were obtained from these fits:

$$a_0^{\mathrm{Z}}/\Lambda^2 = 0.001^{+0.009}_{-0.007} \pm 0.002 \qquad a_{\mathrm{c}}^{\mathrm{Z}}/\Lambda^2 = 0.010^{+0.017}_{-0.027} \pm 0.006\,,$$

$$a_0^{\mathrm{W}}/\Lambda^2 = 0.001 \pm 0.014 \pm 0.004 \qquad a_{\mathrm{c}}^{\mathrm{W}}/\Lambda^2 = 0.000 \pm 0.038 \pm 0.009\,,$$

where the first error was statistical and the second systematic. In each measurement the systematic error was much smaller than the statistical uncertainty. The fitted couplings were found to be in good agreement with the Standard Model expectations of zero, and the corresponding 95% C.L. limits are listed in Table 7.5.

I also performed two-parameter fits to the two pairs of couplings describing the $\mathrm{ZZ}\gamma\gamma$ and $\mathrm{W^+W^-}\gamma\gamma$ vertices. In these fits, the two chosen couplings were allowed to vary simultaneously while the other pair was fixed to the Standard Model value of zero. Figure 7.24 shows the derived 95% C.L. contours which correspond to a change of 3.0 in the negative log-likelihood with respect to its minimum. The fitted parameters were found to be strongly correlated, with correlation coefficients of −56% and −70% for the $\{a_0^{\mathrm{Z}}, a_{\mathrm{c}}^{\mathrm{Z}}\}$ and $\{a_0^{\mathrm{W}}, a_{\mathrm{c}}^{\mathrm{W}}\}$ pairs of couplings, respectively. The limits obtained from the two-parameter fits are

$$-0.018\ \mathrm{GeV}^{-2} < a_0^{\mathrm{Z}}/\Lambda^2 < 0.030\ \mathrm{GeV}^{-2} \quad -0.062\ \mathrm{GeV}^{-2} < a_{\mathrm{c}}^{\mathrm{Z}}/\Lambda^2 < 0.051\ \mathrm{GeV}^{-2},$$

$$-0.049\ \mathrm{GeV}^{-2} < a_0^{\mathrm{W}}/\Lambda^2 < 0.048\ \mathrm{GeV}^{-2} \quad -0.135\ \mathrm{GeV}^{-2} < a_{\mathrm{c}}^{\mathrm{W}}/\Lambda^2 < 0.137\ \mathrm{GeV}^{-2}.$$

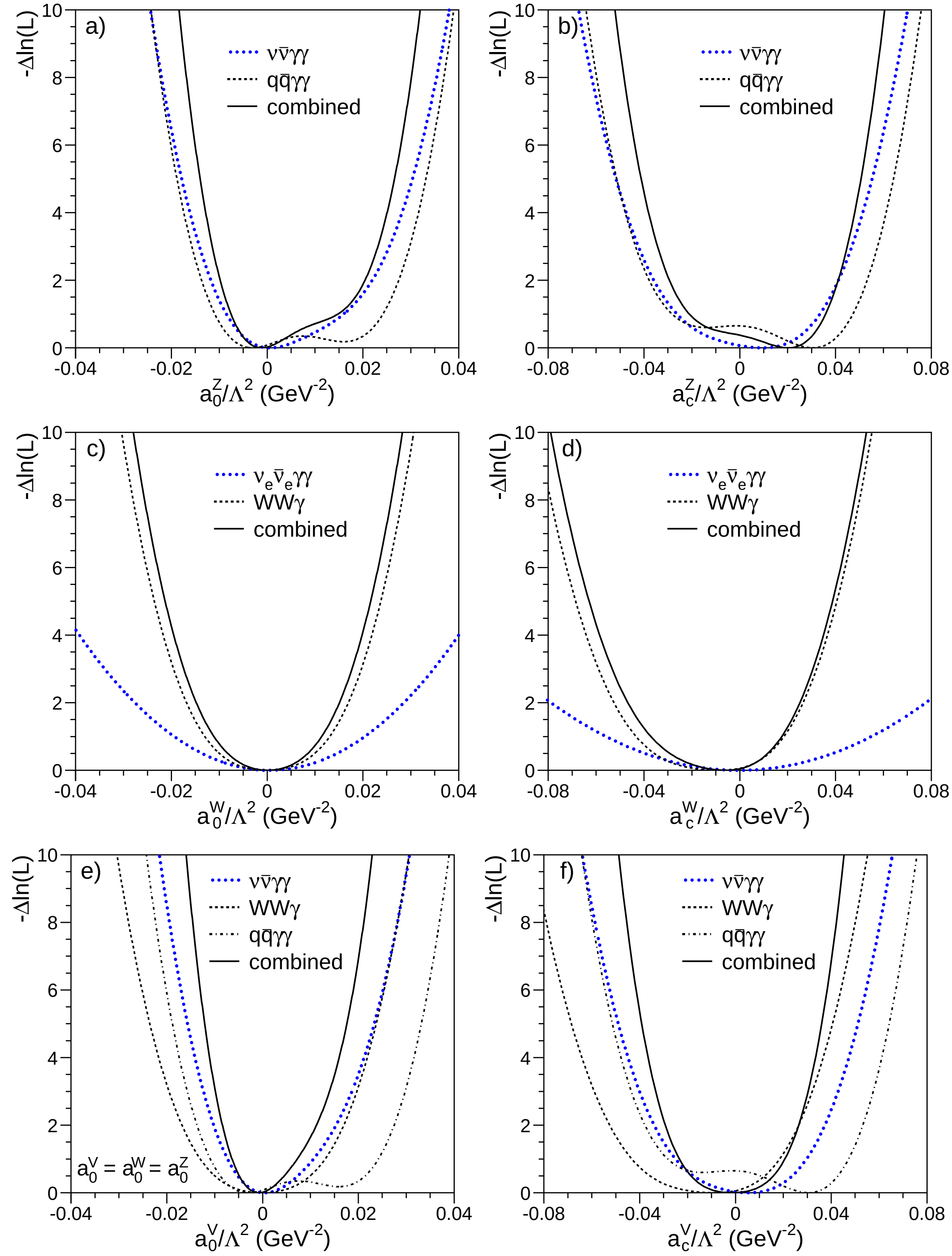

Figure 7.23: The negative log-likelihood functions of the fits for anomalous QGC. All likelihood curves include the effects of systematic uncertainties and correspond to the case where only the coupling in question is allowed to vary from zero. Contributions from different channels are indicated.

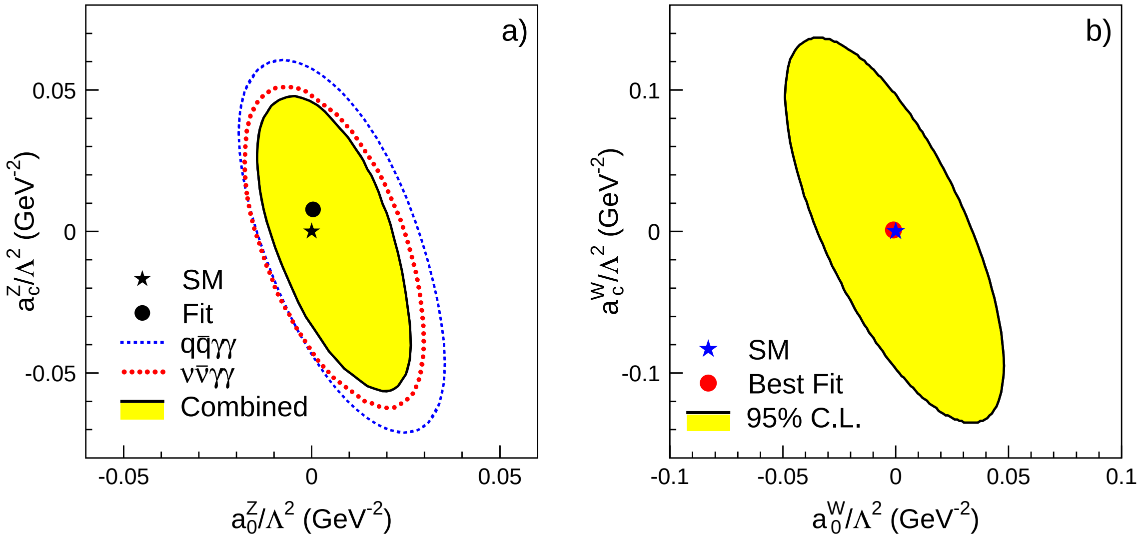

Figure 7.24: The 95% C.L. contours from the two-parameter fits for anomalous QGCs in a) $\{a_0^{\rm Z}, a_{\rm c}^{\rm Z}\}$ and b) $\{a_0^{\rm W}, a_{\rm c}^{\rm W}\}$ planes. In plot a) the results from the $\nu\bar{\nu}\gamma\gamma$ and $\rm q\bar{q}\gamma\gamma$ channels and the combined contour are shown separately.

Combination with Other L3 results

Limits on anomalous quartic couplings have also been obtained by L3 from studies of two other production processes. The $\rm e^+e^- \rightarrow W^+W^-\gamma$ process is sensitive to anomalous contributions from the s-channel photon exchange diagram containing the $\rm W^+W^-\gamma\gamma$ vertex [208], whereas the $\rm e^+e^- \rightarrow q\bar{q}\gamma\gamma$ process can be used to search for anomalous $\rm ZZ\gamma\gamma$ couplings [209]. In this case the anomalous QGC diagram is the same as the one shown in Figure 7.20b, except that the Z boson decays into quarks. These two analyses also found no deviations from the Standard Model. The obtained limits on anomalous QGCs are listed in Table 7.5.

The $\nu\bar{\nu}\gamma\gamma$, $\rm q\bar{q}\gamma\gamma$, and $\rm W^+W^-\gamma$ channels were combined by adding together the corresponding log-likelihoods as shown in Figure 7.23. No significant sources of correlated systematic uncertainties between the three channels were found.

The individual and combined one-parameter likelihood curves for the couplings $\{a_0^{\rm Z}, a_{\rm c}^{\rm Z}\}$ are shown in Figures 7.23a,b. The $\nu\bar{\nu}\gamma\gamma$ and $\rm q\bar{q}\gamma\gamma$ analyses were found to have almost the same sensitivity to these anomalous QGCs. This combination gave

Process	Coupling	95% C.L. Limit
$e^+e^- \to \nu\bar{\nu}\gamma\gamma$	a_0^Z	$-0.012\,\mathrm{GeV}^{-2} < a_0^Z/\Lambda^2 < 0.022\,\mathrm{GeV}^{-2}$
	a_c^Z	$-0.035\,\mathrm{GeV}^{-2} < a_c^Z/\Lambda^2 < 0.041\,\mathrm{GeV}^{-2}$
	a_0^W	$-0.027\,\mathrm{GeV}^{-2} < a_0^W/\Lambda^2 < 0.028\,\mathrm{GeV}^{-2}$
	a_c^W	$-0.077\,\mathrm{GeV}^{-2} < a_c^W/\Lambda^2 < 0.076\,\mathrm{GeV}^{-2}$
$e^+e^- \to q\bar{q}\gamma\gamma$	a_0^Z	$-0.014\,\mathrm{GeV}^{-2} < a_0^Z/\Lambda^2 < 0.027\,\mathrm{GeV}^{-2}$
	a_c^Z	$-0.037\,\mathrm{GeV}^{-2} < a_c^Z/\Lambda^2 < 0.053\,\mathrm{GeV}^{-2}$
$e^+e^- \to W^+W^-\gamma$	a_0^W	$-0.017\,\mathrm{GeV}^{-2} < a_0^W/\Lambda^2 < 0.017\,\mathrm{GeV}^{-2}$
	a_c^W	$-0.052\,\mathrm{GeV}^{-2} < a_c^W/\Lambda^2 < 0.026\,\mathrm{GeV}^{-2}$

Table 7.5: Summary of the 95% C.L. limits on the anomalous quartic couplings obtained by L3 from studies of three different production processes at LEP2. All limits were derived using one-parameter fits, and the systematic uncertainties were taken into account.

the following 95% C.L. limits on the $ZZ\gamma\gamma$ couplings:

$$-0.010\ \mathrm{GeV}^{-2} < a_0^Z/\Lambda^2 < 0.020\ \mathrm{GeV}^{-2},$$

$$-0.029\ \mathrm{GeV}^{-2} < a_c^Z/\Lambda^2 < 0.041\ \mathrm{GeV}^{-2}.$$

The two-parameter fits to the $ZZ\gamma\gamma$ couplings were also combined. The obtained 95% C.L. contour is shown in Figure 7.24a.

In the case of the $W^+W^-\gamma\gamma$ couplings, the inclusion of the $e^+e^- \to W^+W^-\gamma$ channel considerably improved the sensitivity of the search [208]. The combined one-parameter likelihood curves are shown in Figures 7.23c,d. The corresponding 95% C.L. limits on anomalous contributions to the $W^+W^-\gamma\gamma$ vertex are

$$-0.015\ \mathrm{GeV}^{-2} < a_0^W/\Lambda^2 < 0.015\ \mathrm{GeV}^{-2},$$

$$-0.046\ \mathrm{GeV}^{-2} < a_c^W/\Lambda^2 < 0.025\ \mathrm{GeV}^{-2}.$$

As suggested in Reference [210], the couplings describing the $ZZ\gamma\gamma$ and $W^+W^-\gamma\gamma$

vertices may be identical, $a_i^{\mathrm{Z}} = a_i^{\mathrm{W}} \equiv a_i^{\mathrm{V}}$. For completeness, this scenario was also investigated. Figures 7.23e,f show the one-parameter likelihood curves obtained by combining the results from the $\nu\bar{\nu}\gamma\gamma$, $\mathrm{q\bar{q}}\gamma\gamma$, and $\mathrm{W^+W^-}\gamma$ channels. The combined likelihoods yielded the following 95% C.L. limits:

$$-0.008\ \mathrm{GeV}^{-2} < a_0^{\mathrm{V}}/\Lambda^2 < 0.011\ \mathrm{GeV}^{-2},$$
$$-0.029\ \mathrm{GeV}^{-2} < a_c^{\mathrm{V}}/\Lambda^2 < 0.026\ \mathrm{GeV}^{-2}.$$

7.4.2 Measurement of Triple Gauge Boson Couplings

The selected sample of single- and multi-photon events may also be used to measure the triple gauge couplings (TGCs) of the W boson. As shown in Figure 7.25, the $\mathrm{W^+W^-}\gamma$ vertex contributes to the $\mathrm{e^+e^-} \rightarrow \nu_{\mathrm{e}}\bar{\nu}_{\mathrm{e}}\gamma(\gamma)$ process through photon production in W-boson fusion. Assuming electromagnetic gauge invariance, this vertex can be described by two CP-conserving couplings, κ_γ and λ_γ [211].

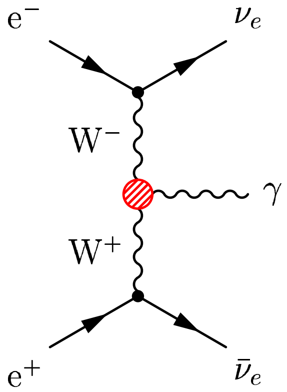

Figure 7.25: Feynman diagram of the WW−fusion $\mathrm{e^+e^-} \rightarrow \nu_{\mathrm{e}}\bar{\nu}_{\mathrm{e}}\gamma$ process.

Deviations from the Standard Model values of $\kappa_\gamma = 1$ and $\lambda_\gamma = 0$ could be detected by studying the photon energy spectrum. In particular, such anomalous couplings were expected to lead to an excess of events with photon energies above those corresponding to the radiative return to the Z. Figure 7.26a shows that the measured energy spectrum was in good agreement with the Standard Model expectation. In particular, in the region of highest sensitivity, $E_\gamma/E_{beam} > 0.86$, 4 events were found in data with 5.8 ± 1.0 events expected from background.

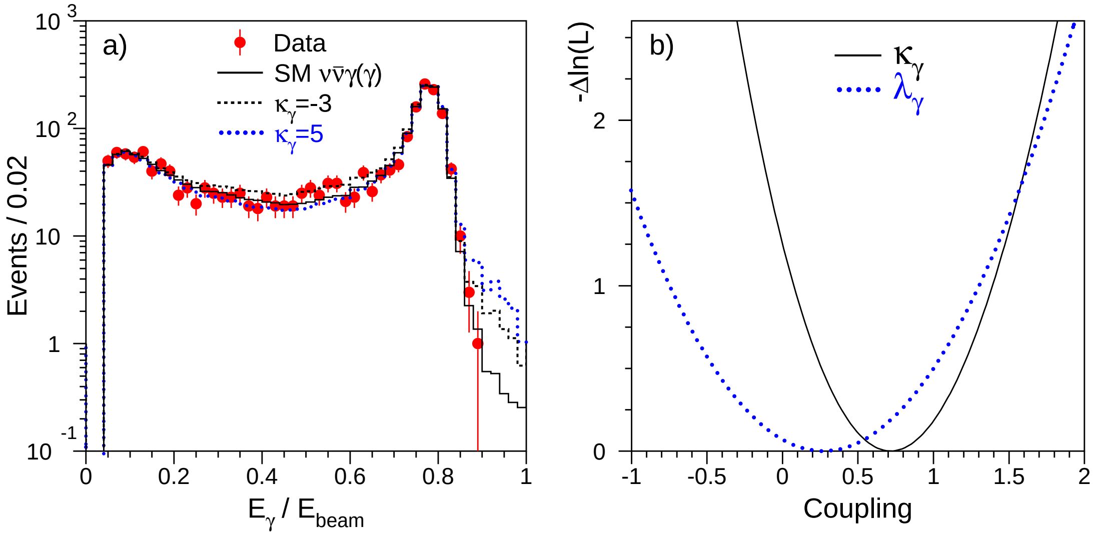

Figure 7.26: a) The energy spectrum of the combined single- and multi-photon sample. The expected effects of anomalous TGCs are also shown for $\kappa_\gamma = -3$ and $\kappa_\gamma = 5$. In each case the λ_γ coupling was set to zero. b) The negative log-likelihood functions for one-parameter fits to κ_γ and λ_γ.

To extract the triple gauge couplings, I used the same methods as in the QGC analysis described in the previous section. The `KKMC` program was used to simulate the Standard Model process $e^+e^- \to \nu\bar{\nu}\gamma(\gamma)$, while the effects of TGC's were estimated using a reweighting procedure from Reference [212]. Figure 7.26b shows the log-likelihood curves obtained from the binned maximum likelihood fits to the photon energy and polar angle. The triple gauge couplings were measured to be

$$\begin{aligned} \kappa_\gamma &= 0.7 \pm 0.5\,(stat) \pm 0.3\,(syst)\,, \\ \lambda_\gamma &= 0.3 \pm 0.7\,(stat) \pm 0.4\,(syst)\,, \end{aligned}$$

in good agreement with the Standard Model prediction of $\kappa_\gamma = 1$ and $\lambda_\gamma = 0$.[23] The systematic uncertainties were dominated by uncertainties on the selection efficiency (see Section 7.1.1), on the $\nu\bar{\nu}\gamma$ cross section [24], and on the TGC modelling [213].

---

[23] A much more precise result was obtained by L3 from a study of W-pair production at LEP2: $\kappa_\gamma = 1.01 \pm 0.07$ and $\lambda_\gamma = -0.02 \pm 0.03$ [202]. However, the W-pair production was also sensitive to the WWZ couplings which could not be disentangled from the WWγ couplings. Moreover, in this study the triple-gauge-boson vertices were tested at a momentum-transfer scale of $Q^2 = s$, while the $\nu\bar{\nu}\gamma$ production occurred at $Q^2 = 0$.